

# A Three-Dimensional Flow Stability Analysis of the Particle Bed Nuclear Reactor

by

**James Kalamas**

S.B. Massachusetts Institute of Technology(1991)

SUBMITTED IN PARTIAL FULFILLMENT OF THE  
REQUIREMENTS FOR THE DEGREE OF

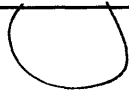
**Master of Science**  
in  
**Aeronautics and Astronautics**  
at the  
**Massachusetts Institute of Technology**

September, 1993

© James Kalamas, 1993. All rights reserved.

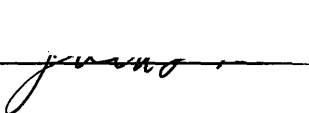
The author hereby grants to MIT permission to reproduce and to  
distribute copies of this thesis document in whole or in part.

Signature of Author



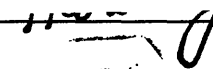
Department of Aeronautics and Astronautics  
July 7, 1993

Certified by



7/8/93  
Professor Jack L. Kerrebrock  
Thesis Supervisor, Department of Aeronautics and Astronautics

Accepted by



Professor Harold Y. Wachman  
Chairman, Department Graduate Committee

**Aero**

MASSACHUSETTS INSTITUTE  
OF TECHNOLOGY

SEP 22 1993

# **A Three-Dimensional Flow Stability Analysis of the Particle Bed Nuclear Reactor**

by

**James Kalamas**

Submitted to the Department of Aeronautics & Astronautics  
on July 7, 1993 in partial fulfillment of the requirements for the  
Degree of Master of Science in Aeronautics & Astronautics.

## **Abstract**

A three-dimensional stability analysis of the particle bed nuclear reactor using perturbation theory is detailed for a plane-parallel approximation of a particle bed fuel element with hydrogen as the propellant. With the introduction of normal mode perturbations to the flow variables, the governing equations of the flow through the particle bed are solved to determine the boundary for stable operation as a function of particle  $Re$  and bed inlet-to-outlet temperature ratio. Using this technique, the stability boundary with no bed thermal conductivity is found to be qualitatively similar to that calculated by previous simplified analyses that assume parallel flow through the bed. With the addition of 2.5 W/mK of bed conductivity, the model indicates increased stability for the low  $Re$  regime ( $Re < 30$ ). Finally, with the introduction of frits, significant stabilization is indicated for this low  $Re$  regime. In all cases examined, the nominal bed operating point of 40 GW/m<sup>3</sup> is found to lie in a stable region.

Thesis Supervisor: Jack L. Kerrebrock

Title: *R. C. Maclaurin Professor of Aeronautics and Astronautics*

## **Acknowledgements**

I wish to thank my thesis advisor Professor Jack Kerrebrock for his guidance during the course of this work. The understanding and freedom which he afforded me made the entire process much more enjoyable and intellectually satisfying than it might otherwise have been. I also wish to thank Tim Lawrence, Jonathan Witter, David Suzuki, Eric Sheppard, Chris Lentz, Ray Sedwick, and Mohanjit Jolly for numerous helpful discussions.

On a more personal side, I am eternally indebted to my family for the many years of love and devotion which they have given me; this work can only serve as a small measure of my appreciation. Finally, I wish to thank Alicia. She has been with me throughout this process and thankfully remains with me now that it is complete. Her love and support have been immeasurably important to me and this work is dedicated to her.

# Table of Contents

<b>Abstract</b>	<b>2</b>
<b>Acknowledgements</b>	<b>3</b>
<b>Nomenclature</b>	<b>7</b>
<b>Chapter 1 Introduction</b>	<b>8</b>
1.1 The Particle Bed Reactor	10
1.2 Overview	14
<b>Chapter 2 Governing Equations for the Particle Bed Reactor</b>	<b>16</b>
<b>Chapter 3 Methods Used in Stability Analysis</b>	<b>20</b>
3.1 Nondimensionalization Procedure	20
3.2 Parallel Stream Analysis	21
3.3 Local Stability Analysis	26
3.4 Complete Stability Analysis	30
3.4.1 Complete Stability Analysis for the Particle Bed Without Frits	31
3.4.2 Complete Stability Analysis for the Particle Bed Including the Cold Frit	36
3.4.3 Complete Stability Analysis for the Particle Bed Including Both Frits	39
<b>Chapter 4 Comparison of Stability Model to Experimental Results</b>	<b>42</b>
<b>Chapter 5 Conclusions and Recommendations for Future Work</b>	<b>45</b>
<b>Appendix A Mathematica Code</b>	<b>47</b>
<b>Bibliography</b>	<b>53</b>

# List of Figures

## Chapter 1

1.1 Schematic diagram of a generic nuclear thermal thruster.	9
1.2 Schematic diagram of a PBR thruster.	11
1.3 Cut-away diagram of a typical fuel element.	12
1.4 Detail of PBR fuel element.	13

## Chapter 2

2.1 Plane-parallel approximation for a PBR fuel element.	17
--	----

## Chapter 3

3.1 Parallel stream stability map.	25
3.2 Parallel stream stability contour map with contours equally spaced by $\partial(\log p)/\partial(\log \mathbf{Re}) = 0.0002$ .	25
3.3 Local stability analysis for PBR at the bed inlet and exit.	29
3.4 Complete stability analysis of particle bed for $k_m=0$ and $2.5 \text{ W/mK}$ .	34
3.5 Radial dependence of perturbation quantities calculated by complete analysis for the case $k_m=0$ , $\omega=0$ , $\phi=13.7$ , $\mathbf{Re}=100$ .	35
3.6 Complete stability analysis of particle bed and cold frit for $k_m=2.5 \text{ W/mK}$ .	38
3.7 Complete stability analysis of particle bed and both frits for $k_m=2.5 \text{ W/mK}$ .	41

## Chapter 4

4.1 Comparison of parallel stream and complete stability models to FIT data.	44
--	----

# List of Tables

## Chapter 1

1.1 Operating parameters for PBR vs. NERVA Composite.	14
---	----

## Nomenclature

<b>b</b>	inertia parameter[m]	<b>Re</b>	Reynolds number based on particle diameter
<b>c</b>	constant pressure specific heat[J/kgK]	<b>S</b>	density-specific heat ratio
<b>d</b>	particle diameter[m]	<b>T</b>	temperature[K]
<b>Da</b>	Darcy number	<b>u</b>	x-component of flow velocity[m/s]
<b>Fs</b>	Forchheimer number	<b>v</b>	y-component of flow velocity[m/s]
<b>I<sub>sp</sub></b>	Specific impulse[s]	<b>w</b>	z-component of flow velocity[m/s]
<b>k</b>	thermal conductivity[W/mK]	<b>γ</b>	specific heat ratio
<b>K</b>	permeability[m <sup>2</sup> ]	<b>ε</b>	porosity
<b>k<sub>x</sub></b>	wavenumber of x-axis perturbation[1/m]	<b>λ</b>	thermal conductivity ratio
<b>k<sub>y</sub></b>	wavenumber of y-axis perturbation[1/m]	<b>μ</b>	viscosity[kg/s m]
<b>k<sub>z</sub></b>	wavenumber of z-axis perturbation[1/m]	<b>ρ</b>	density[kg/m <sup>3</sup> ]
<b>ℓ</b>	bed thickness[m]	<b>φ</b>	bed temperature ratio
<b>M</b>	Mach number	<b>ω</b>	perturbation growth rate[1/s]
<b>n</b>	exponent for viscosity temperature dependence	<b>( )<sub>i</sub></b>	inlet conditions
<b>p</b>	pressure[N/m <sup>2</sup> ]	<b>( )<sub>o</sub></b>	zeroth order quantities
<b>Pr</b>	Prandtl number	<b>( )<sub>x</sub></b>	perturbation amplitudes as a function of x
<b>q</b>	volumetric heat addition[W/m <sup>3</sup> ]	<b>( )'</b>	first order quantities
<b>R</b>	gas constant[J/kgK]		

# Chapter 1

## Introduction

The development of nuclear thermal propulsion(NTP) for space applications began with the ROVER/NERVA program in the mid 1950's. This program resulted in the design, construction, and testing of 20 reactors and lasted until 1973 at which point funding was stopped. Interest in NTP was rekindled in 1990 with President George Bush's Space Exploration Initiative(SEI) which included among its goals a manned mission to Mars by the year 2016. For such a mission nuclear propulsion is highly advantageous and several designs have been proposed including solid core reactors(similar to the NERVA design), gaseous nuclear rockets, and particle bed reactors(the focus of this work).

The basic principle of NTP is the conversion of thermal energy into kinetic energy. To accomplish this, hydrogen propellant at high pressure(30-60 atm) is passed through a nuclear reactor core where it is heated to high temperature(2000-3000 K) and exhausted at high speed through a converging-diverging nozzle. A schematic of a generic design is given in Figure 1.1. By employing such a design, many advantages over chemical and other forms of propulsion may be realized. The high temperatures to which the propellant( $H_2$ ) is raised and its low molecular weight give  $I_{sp}$  's in the 850 - 1000 s range resulting in shorter trip time, which in the case of manned missions is paramount for minimizing crew exposure to background radiation encountered in space.



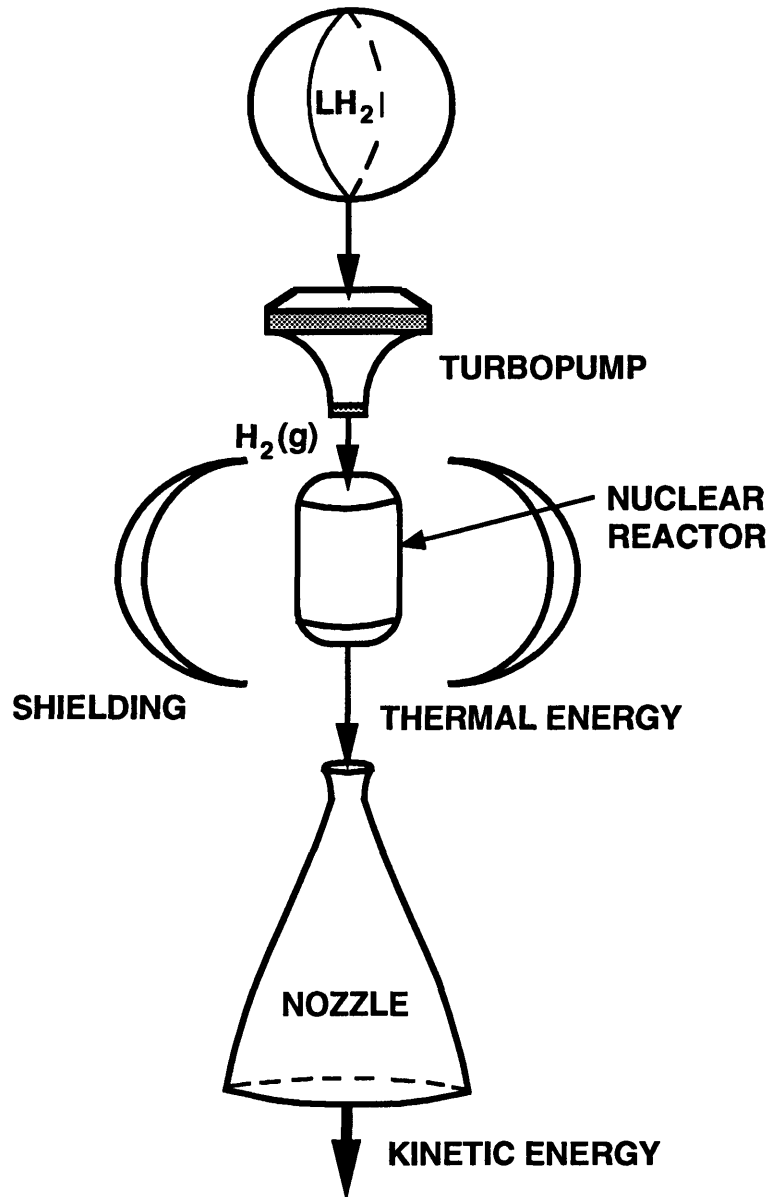


**Figure 1.1 Schematic diagram of a generic nuclear thermal thruster.**

Also, the large power density possible with hydrogen cooling allows for engine designs with high thrust- to-weight ratios(4-20 neglecting shielding). With thrust-to-weight ratios in this range, reductions in initial mass to low earth orbit for lunar and martian missions of 35% and 50-65% respectively may be realized. <sup>1</sup>

## 1.1 The Particle Bed Reactor

One of the more promising designs for fulfilling the SEI goals is the particle bed reactor(PBR) which has been the focus of much research recently. A schematic diagram of a PBR thruster is shown in Figure 1.2. The reactor itself consists of a set of cylindrical fuel elements encased in hexagonal moderator blocks of graphite(beryllium in some designs) assembled within the chamber of the thruster. Hydrogen is introduced into the chamber at high pressure, distributed to the various fuel elements through the inlet plenum, heated within the fuel elements, and exhausted at high velocity via the outlet plenum through a converging-diverging nozzle.

A cut-away diagram of a typical fuel element is shown in Figure 1.3 with a similar element shown in cross section in Figure 1.4. From Figure 1.3, the hydrogen passes through inlet pipes within the moderator material and is introduced uniformly into each element via the inlet plenum. A typical element (See Figure 1.4) consists of a number of spherical fuel particles packed within the annular region between porous cold and hot frits. The fuel particles are nominally 0.5 mm in diameter and consist of a core of UC<sub>2</sub> surrounded by successive layers of pyrolytic carbon(PyC) and ZrC. The hydrogen passes radially through the cold frit at low temperature, is heated by the energy release from the fuel particles, passes through the hot frit, and exits axially down the central channel of the fuel element into the outlet plenum.

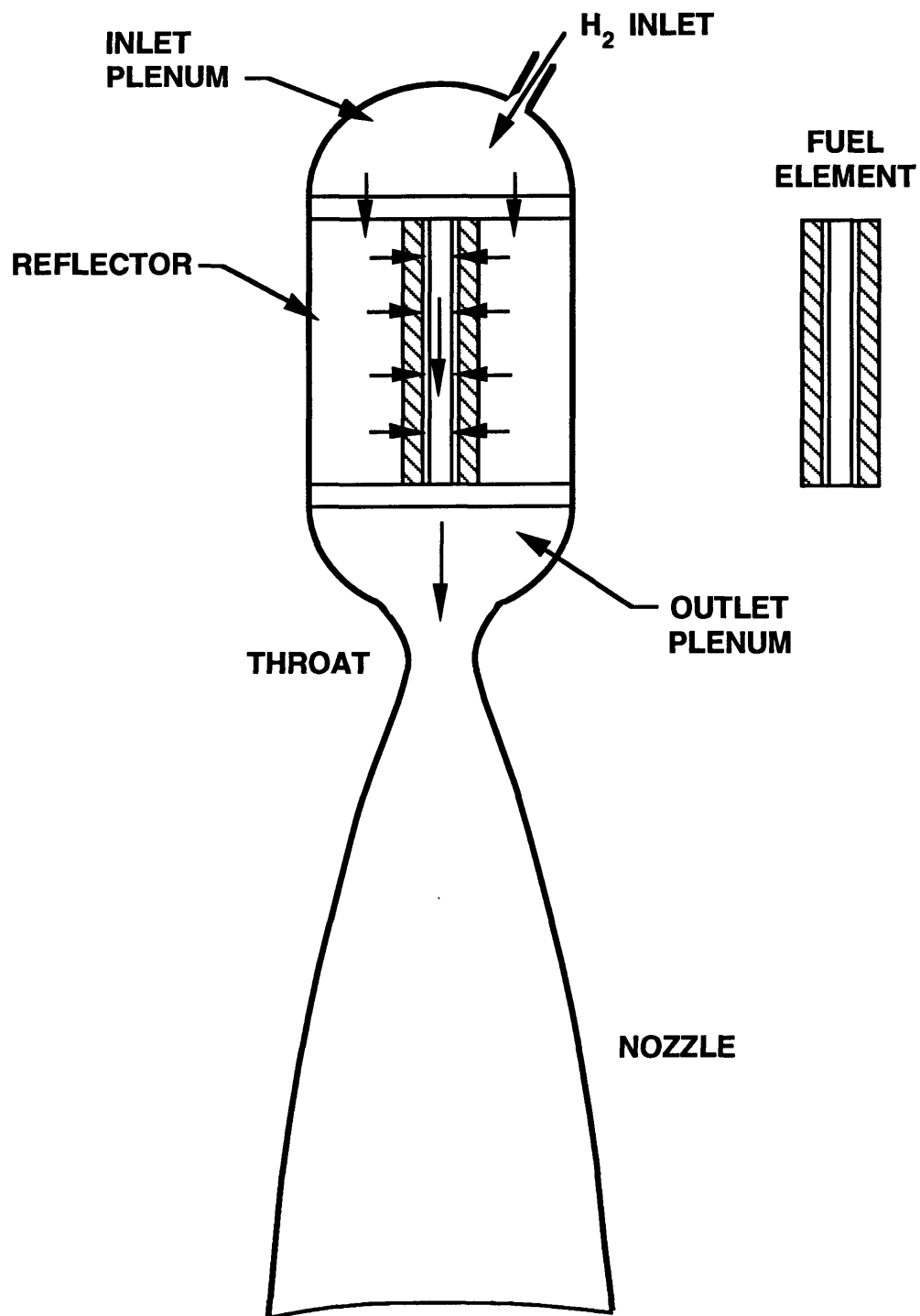
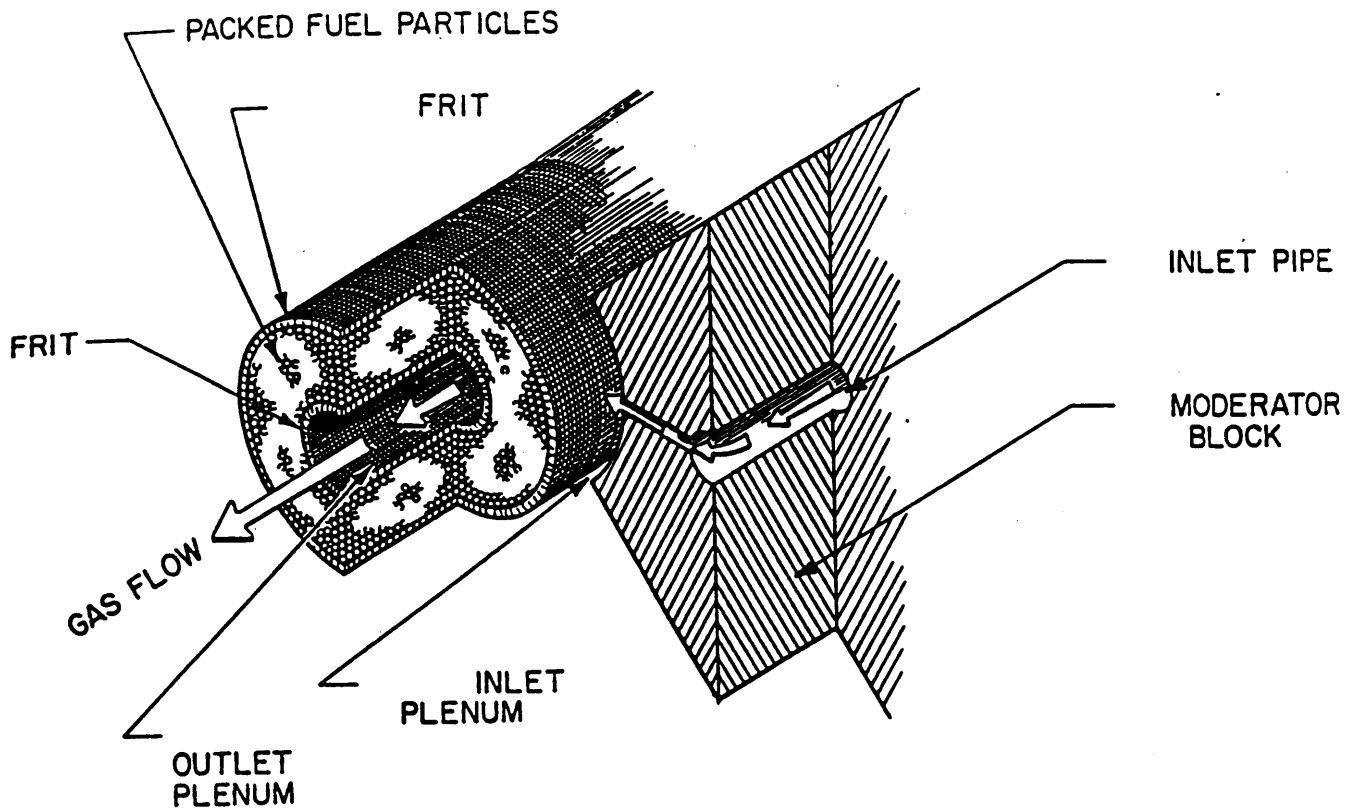
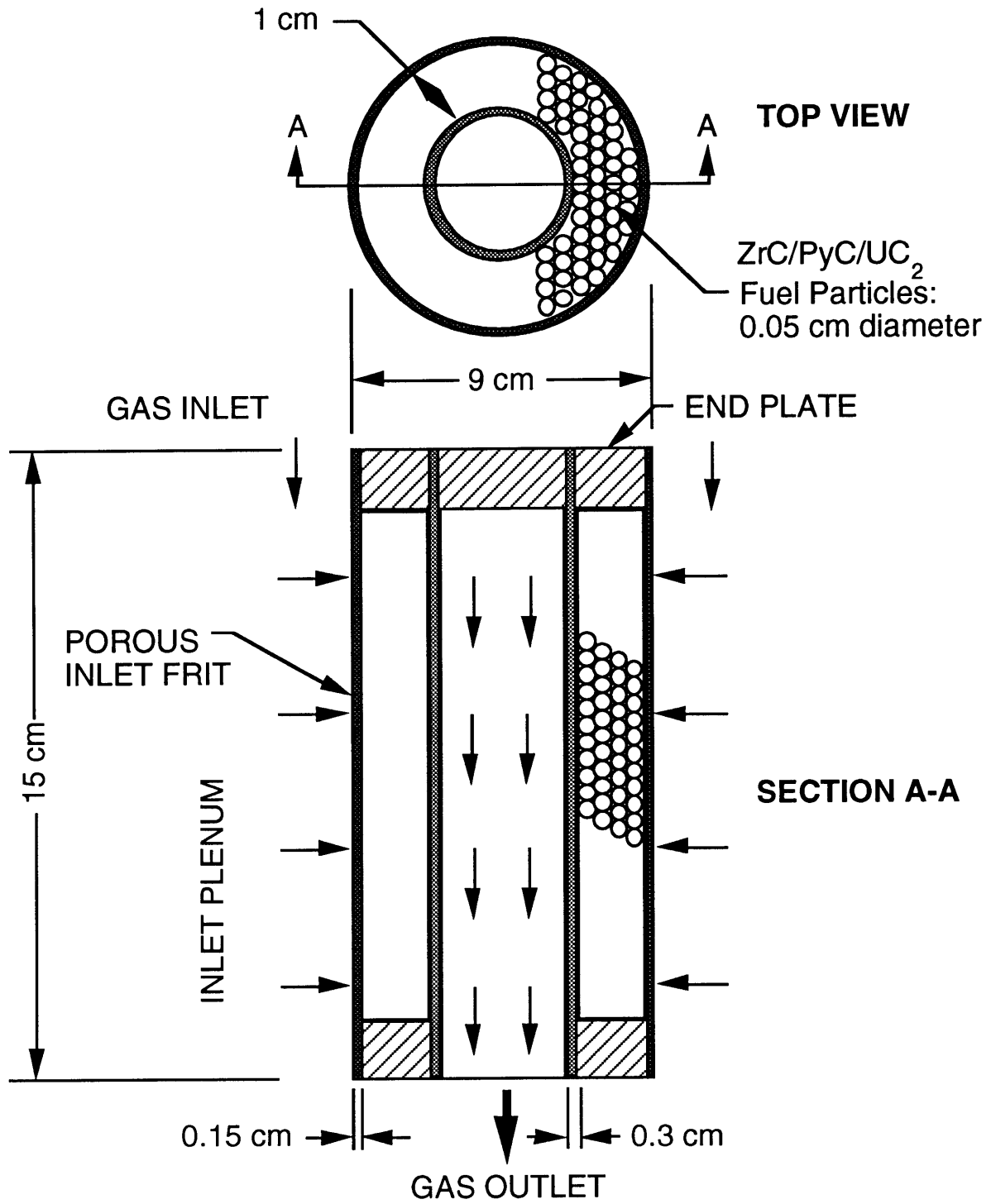


Figure 1.2 Schematic diagram of a PBR thruster.



**Figure 1.3 Cut-away diagram of a typical fuel element. <sup>2</sup>**

The PBR offers several advantages over other reactor designs. The small size of the particles provides a large surface area for heat transfer to the propellant which in turn gives high power densities(20-80 GW/m<sup>3</sup>). These large power densities allow for the design of small, low-mass reactors which are easier to shield(50% less shielding than NERVA) and allow for redundant engines for higher system reliability. The direct particle cooling by the propellant gives high exit gas temperatures(>3000 K) while the plenum nature of the design maintains the moderator and most of the structural elements



**Figure 1.4 Detail of PBR Fuel Element**

at propellant inlet temperatures(<300 K). Compared to an updated NERVA design, the PBR offers similar thrust and  $I_{sp}$  with much smaller size and mass(See Table 1.1).

**Table 1.1 Operating Parameters for PBR vs. NERVA Composite(from Nuclear Thermal Propulsion Workshop-July, 1990).**

	<b>PBR BASELINE <sup>3</sup></b>	<b>NERVA COMPOSITE <sup>4</sup></b>
Thrust(N)	334,000	334,000
Specific Impulse(s)	971	925
Thrust/Weight w/o shield(N/kg)	20	4
Pressure(atm)	60	60
Gas Exit Temperature(K)	3200	2700
Power Density(GW/m <sup>3</sup> )	40	1.5

With all the benefits listed above, a possible problem with the PBR design is flow instability during operation. A plausible mode of instability may be envisioned in the case of a flow perturbation. If a perturbation to the flow occurs causing a localized reduction in propellant mass flow, the particles in this region will become hotter than those in the bulk of the element. As the temperature rises, the viscosity of the hydrogen will increase and consequently the resistance to flow in this region will also increase. With increased resistance, more flow will tend to divert from this region, and the element will experience thermal runaway until failure.

## 1.2 Overview

To explore the issue of stability, this work utilizes three techniques to determine the regions of stable and unstable operation for a particle bed reactor. These include a

one-dimensional approximation(parallel stream model), a three-dimensional local stability analysis using perturbation theory, and a complete stability analysis similar to the local analysis including the boundary conditions on the particle bed along with the effects of the cold and hot frits. Finally, the complete model is compared to experimental data and conclusions and recommendations for future work are offered. The three dimensional governing equations of flow through a parallel plane fuel element are given in Chapter 2. Chapter 3 outlines the methods used for stability analysis, while comparisons to experimental data and conclusions and recommendations are offered in Chapters 4 and 5 respectively.

## Chapter 2

### Governing Equations for the Particle Bed Reactor

In this work the fuel element is modelled as a plane-parallel isotropic homogeneous porous bed matrix(See Figure 2.1). The governing equations for a compressible convective fluid passing through such an element are adapted from Prasad *et. al.* <sup>5</sup> and presented below.

$$\text{State} \quad p = \rho RT \quad (2.1)$$

$$\text{Continuity} \quad \frac{\partial \rho}{\partial t} + \frac{\partial}{\partial x}(\rho u) + \frac{\partial}{\partial y}(\rho v) + \frac{\partial}{\partial z}(\rho w) = 0 \quad (2.2)$$

$$\text{Momentum} \quad \text{x:} \quad \frac{\rho}{\varepsilon} \frac{\partial u}{\partial t} = -\frac{\partial p}{\partial x} - \frac{\mu_i}{K} \left( \frac{T}{T_i} \right)^n u - \frac{\rho b}{K} |\vec{V}| u \quad (2.3a)$$

$$\text{y:} \quad \frac{\rho}{\varepsilon} \frac{\partial v}{\partial t} = -\frac{\partial p}{\partial y} - \frac{\mu_i}{K} \left( \frac{T}{T_i} \right)^n v - \frac{\rho b}{K} |\vec{V}| v \quad (2.3b)$$

$$\text{z:} \quad \frac{\rho}{\varepsilon} \frac{\partial w}{\partial t} = -\frac{\partial p}{\partial z} - \frac{\mu_i}{K} \left( \frac{T}{T_i} \right)^n w - \frac{\rho b}{K} |\vec{V}| w \quad (2.3c)$$

$$\text{Energy} \quad (\rho c)_m \frac{\partial T}{\partial t} + \rho c \left( u \frac{\partial T}{\partial x} + v \frac{\partial T}{\partial y} + w \frac{\partial T}{\partial z} \right) = k_m \left( \frac{\partial^2 T}{\partial x^2} + \frac{\partial^2 T}{\partial y^2} + \frac{\partial^2 T}{\partial z^2} \right) + q \quad (2.4)$$



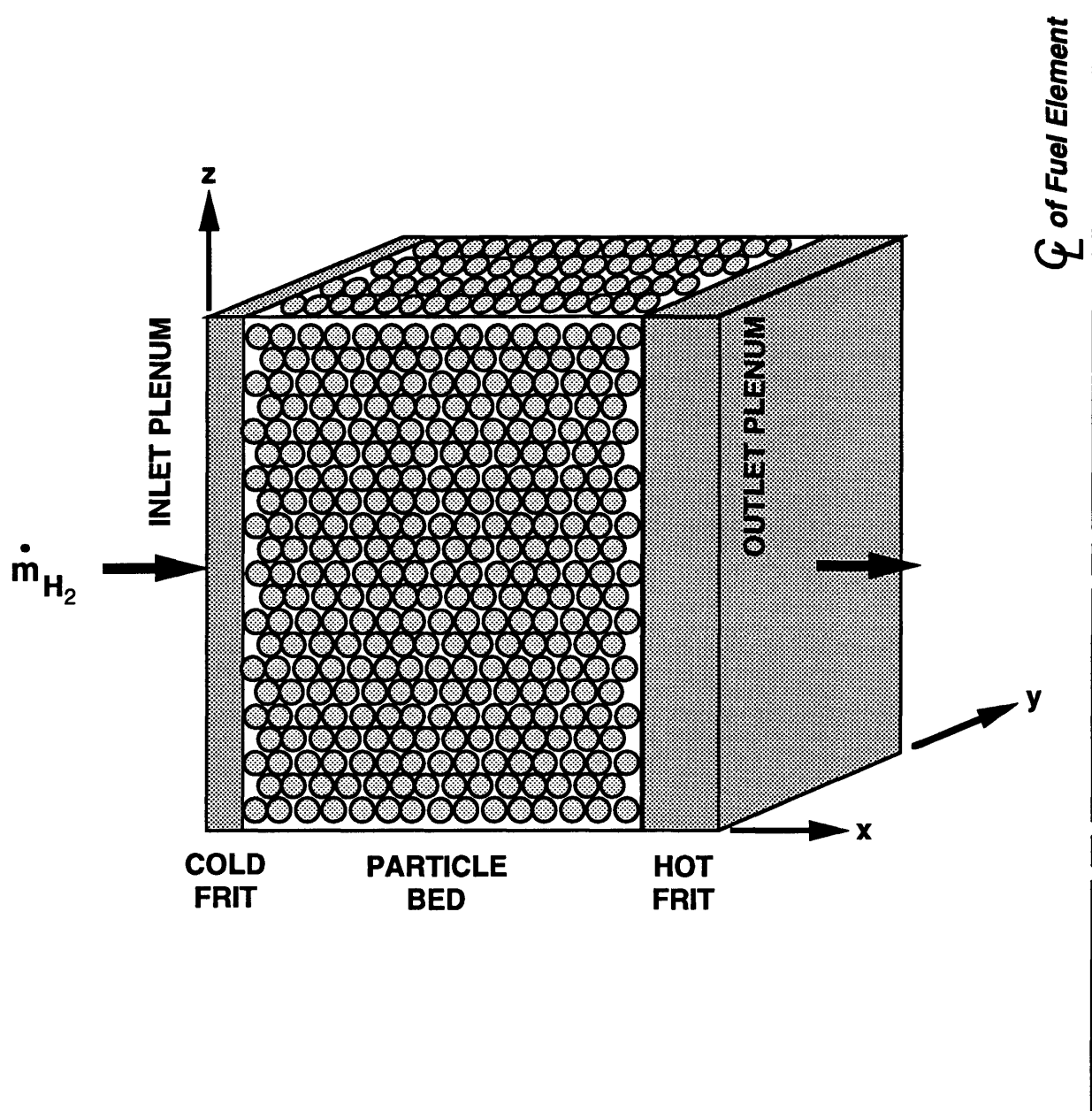


Figure 2.1 Plane-parallel approximation for a PBR fuel element.

The above equations include the familiar fluid quantities of pressure(p), temperature(T), density( $\rho$ ), gas constant(R), specific heat(c), and velocity(magnitude  $|\vec{V}|$  and components u, v, w in the x, y, and z directions respectively) along with the bed matrix properties of porosity( $\epsilon$ ), permeability(K), inertia parameter(b), density of the particles( $\rho_m$ ), specific heat of the particles( $c_m$ ), effective thermal conductivity of the bed matrix( $k_m$ ), and volumetric heat addition from the bed to the fluid(q). The permeability and inertia parameter are functions of the porosity and are given by <sup>6</sup>

$$K = \frac{\epsilon^3 d^2}{150(1-\epsilon)^2} \quad (2.5)$$

$$b = \frac{1.75\sqrt{K}}{\sqrt{150}\epsilon^{1.5}} \quad (2.6)$$

Included in the momentum equations is the temperature dependence of the viscosity of the fluid( $\mu$ ) which, for hydrogen, follows the functional form <sup>7</sup>

$$\mu(T) = \mu_i \left( \frac{T}{T_i} \right)^n \quad (2.7)$$

where  $\mu_i$  is the viscosity at the bed inlet with  $T_i$  the inlet temperature and  $n=2/3$  for hydrogen over a temperature range of 300-3000 K.

The bed properties are found in the final two terms of the momentum equations and represent the Forchheimer & Brinkman modification to Darcian flow. Simply stated, the first of these terms represents laminar flow(Darcian flow) through a porous bed while the second term accounts for turbulent flow. For laminar flow, the pressure drop through the bed is proportional to the velocity of the flow; however, for turbulent flow the boundary layer around the particles becomes significant. In this situation an "inertial core" appears outside these particle boundary layers, and in this region the pressure drop

is proportional to the square of the flow velocity.

Several assumptions have been made in the formulation of the flow equations. In the case of the momentum equations, gravity terms are assumed negligible since the bed thickness is small (1 cm) and the fluid is a gas (hydrogen), shear stress is neglected as a minor effect compared to the Forchheimer-Brinkman term, and the convective portion of the fluid acceleration ( $[\vec{V} \cdot \nabla] \vec{V}$ ) is considered small in porous media.<sup>8</sup> For the energy equation, the substantial derivative of pressure and the viscous stress term are assumed small and the particle and fluid temperatures are assumed equal. Throughout the analyses which follow, the bed porosity is assumed uniform, and all specific heats and thermal conductivities are held fixed at their bed inlet values.

## Chapter 3

### Methods Used in Stability Analysis

The stability boundaries for the particle bed reactor were determined using three increasingly complex methods: parallel stream model, local stability analysis, and complete stability analysis. The parallel stream model is similar to the formalism of Bussard and DeLauer<sup>9</sup> in that only the radial flow through the reactor element is considered. Using this assumption, the pressure drop through the bed is calculated at the bed exit with respect to the particle Reynolds number with a positive change of pressure drop with increasing mass flow indicating instability. In the local stability analysis, Equations 2.1 - 2.4 are linearized and a harmonic perturbation is introduced for each of the flow variables. The growth rate of this perturbation is then calculated for a range of perturbation wavenumbers at the inlet and exit to the bed. A positive growth rate indicates instability with stability indicated by a negative growth rate. Finally, the complete stability analysis includes the radial dependence of the perturbations with boundary conditions imposed at the bed inlet and exit. The effects of the cold and hot frits are also included in this analysis.

#### 3.1 Nondimensionalization Procedure

To facilitate manipulation of the equations used in the various analyses herein, flow properties are nondimensionalized using the bed input flow quantities  $p_i$ ,  $\rho_i$ ,  $T_i$ , and

$u_i$ , length scales are nondimensionalized by the particle diameter( $d$ ), and the following dimensionless parameters are introduced:

$$\text{Reynolds Number} \quad \mathbf{Re} = \frac{\rho_i u_i d}{\mu_i} \quad (3.1)$$

$$\text{Forchheimer Number} \quad \mathbf{Fs} = \frac{b}{d} \quad (3.2)$$

$$\text{Darcy Number} \quad \mathbf{Da} = \frac{K}{d^2} \quad (3.3)$$

$$\text{Temperature Ratio} \quad \phi = \frac{T_o(\text{exit}) - T_i}{T_i} \quad (3.4)$$

$$\text{Prandtl Number} \quad \mathbf{Pr} = \frac{\mu_i c}{k} \quad (3.5)$$

$$\text{Specific Heat Ratio} \quad \mathbf{S} = \frac{(\rho c)_m}{\rho_i c} \quad (3.6)$$

$$\text{Thermal Conductivity Ratio} \quad \lambda = \frac{k_m}{k} \quad (3.7)$$

To distinguish between dimensional and nondimensional parameters, all nondimensional variables and parameters will be indicated in bold face throughout this presentation.

### 3.2 Parallel Stream Analysis

In the parallel stream analysis, the flow properties are assumed to only vary radially( $x$ -axis), thus Equations 2.1-2.4 are approximated to zeroth order by the

following, with the zeroth order quantities(x-dependent quantities) indicated by the subscript "o".

$$\text{State} \quad p_o = \rho_o R T_o \quad (3.8)$$

$$\text{Continuity} \quad \frac{d}{dx}(\rho_o u_o) = 0 \quad (3.9)$$

$$\text{Momentum} \quad \frac{dp_o}{dx} + \frac{\mu_i}{K} \left( \frac{T_o}{T_i} \right)^n u_o + \frac{b}{K} \rho_o u_o^2 = 0 \quad (3.10)$$

$$\text{Energy} \quad \rho_o u_o c \frac{dT_o}{dx} = k_m \frac{d^2 T_o}{dx^2} + q \quad (3.11)$$

Integration of the above set of equations yields the zeroth order solutions to the governing equations of the flow. For the zeroth order solutions used in this and later analyses, the second derivative of temperature with respect to the x-direction in Equation 3.11 has been neglected for simplicity. By making this approximation, integration of Equation 3.11 from the bed inlet to exit yields the following relationship between  $q$ ,  $Re$ , and  $\phi$  at the bed inlet:

$$q = \frac{\phi Re c T_i \mu_i}{\ell d} \quad (3.12)$$

where  $\ell$  is the thickness of the bed. This relationship will prove important in the analyses which follow.

Using the nondimensionalization procedure from Section 3.1, Equations 3.8 - 3.11 become:

$$\text{State} \quad p_o = \rho_o T_o \quad (3.13)$$

$$\text{Continuity} \quad \frac{d}{dx}(\rho_o u_o) = 0 \quad (3.14)$$

$$\text{Momentum} \quad \frac{dp_o}{dx} = -\frac{\gamma M_i^2}{p_o} \left[ \frac{1}{\text{Re Da}} T_o^{(n+1)} + \frac{\text{Fs}}{\text{Da}} T_o \right] \quad (3.15)$$

$$\text{Energy} \quad (\rho_o u_o) \frac{dT_o}{dx} = \frac{d}{\ell} \phi \quad (3.16)$$

where  $\gamma$  is the specific heat ratio for hydrogen at the inlet and  $M_i$  is the Mach number at the bed inlet. The inlet Mach number may be derived using the speed of sound at the inlet along with Equation 3.12 to give

$$M_i = \frac{\gamma - 1}{\gamma} \frac{q_o \ell}{\phi p_i \sqrt{\gamma R T_i}} \quad (3.17)$$

Using Equations 3.13-3.16, the zeroth order solutions as well as the derivatives of the zeroth order quantities with respect to  $x$  may be calculated. Looking at continuity first, integration of Equation 3.14 yields

$$u_o = \frac{1}{\rho_o} \quad (3.18)$$

Substitution of this result into Equation 3.16 gives

$$\frac{dT_o}{dx} = \frac{d}{\ell} \phi \quad (3.19)$$

and upon integration, Equation 3.19 becomes

$$T_o = \frac{d}{\ell} \phi x + 1 \quad (3.20)$$

Expansion of Equation 3.14 gives the zeroth order velocity gradient and differentiation of Equation 3.13 yields after some manipulation the corresponding gradient for density.

Both relations are as follows:

$$\frac{du_o}{dx} = -\frac{1}{\rho_o^2} \frac{d\rho_o}{dx} \quad (3.21)$$

$$\frac{d\rho_o}{dx} = \frac{1}{T_o} \left( \frac{dp_o}{dx} - \frac{d}{\ell} \rho_o \phi \right) . \quad (3.22)$$

Finally, substituting Equation 3.20 into Equation 3.15 and integrating gives

$$p_o^2 = 1 - \gamma M_i^2 \left\{ \frac{3}{4} \frac{\ell}{d \phi \mathbf{Re} \mathbf{Da}} \left[ \left( \frac{d}{\ell} \phi \mathbf{x} + 1 \right)^{(n+2)} - 1 \right] + \frac{\ell \mathbf{Fs}}{d \phi \mathbf{Da}} \left[ \left( \frac{d}{\ell} \phi \mathbf{x} + 1 \right)^2 - 1 \right] \right\} \quad (3.23)$$

which is the zeroth order pressure as a function of x through the bed.

In the parallel stream analysis, the stability of the reactor is determined by calculating the pressure at the bed exit as a function of Reynolds number. The inlet pressure to the bed is fixed throughout the analysis and q is assumed constant through the bed. Instability is indicated if with increasing mass flow the pressure at the exit increases. The input parameters for the analysis are as follows:  $p_i = 60$  atm,  $T_i = 300$  K,  $d = 0.0005$  m,  $\varepsilon = 0.4$ ,  $c = 14,600$  J/kg K,  $\gamma = 1.409$ ,  $\mu_i = 9 \times 10^{-6}$  kg/s m, and  $R = 4,157$  J/kg K. With these input parameters, the pressure change with respect to  $\mathbf{Re}$  at the bed exit was calculated using Equation 3.23. The results are plotted in Figure 3.1 with the pressure derivative given by  $\partial(\log p_{\text{exit}}) / \partial(\log \mathbf{Re})$  for a range of  $\mathbf{Re}$  and  $\phi$ . From Figure 3.1, the region of instability occurs at low  $\mathbf{Re}$  and large  $\phi$ . These trends become more apparent in the contour plot generated from Figure 3.1 and are presented in Figure 3.2. The neutral stability boundary is indicated by the zero pressure gradient contour with increasing stability to the right of this contour and increasing instability above this curve.



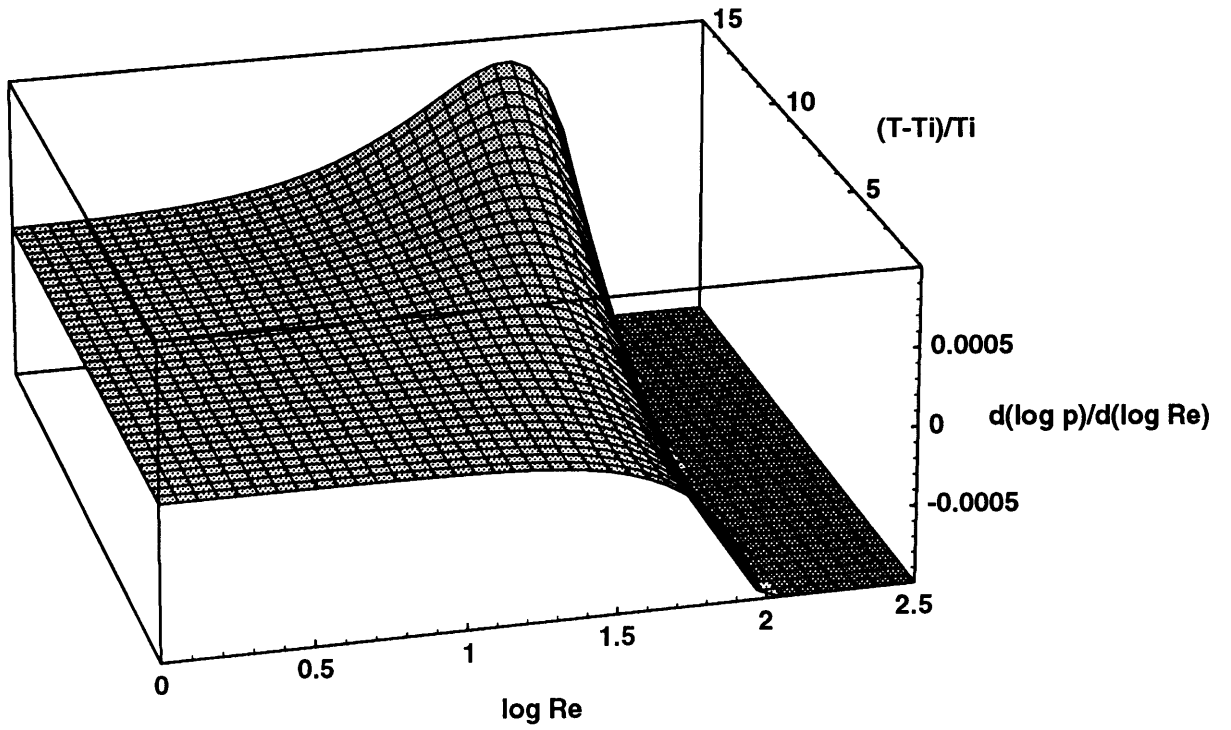


Figure 3.1 Parallel stream stability map.

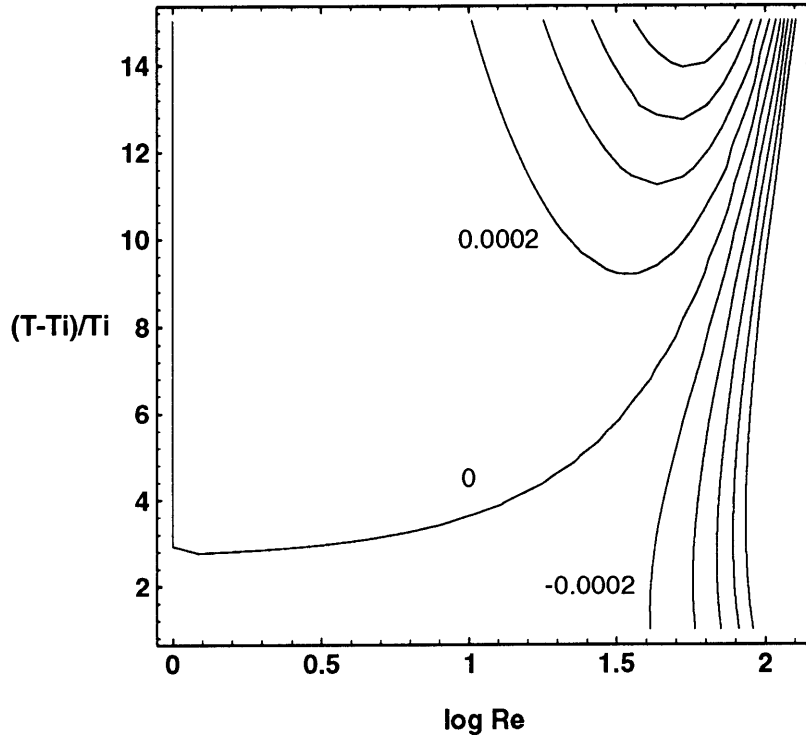


Figure 3.2 Parallel stream stability contour map with contours equally spaced by  $\partial(\log p)/\partial(\log Re) = 0.0002$ .

The neutral stability boundary generated by the parallel stream model is qualitatively very similar to the boundary generated by Bussard & DeLauer<sup>9</sup>, Maise's modification to Bussard & DeLauer<sup>7</sup>, and the analysis by Witter<sup>10</sup>. It should be noted, however, that the curves do not exactly coincide. In the Bussard & DeLauer analysis, the assumption is initially made that the inlet-to-outlet pressure ratio is one; that is, the pressure drop through the bed is assumed negligible. With this assumption, the density of the flow becomes proportional to the inverse of T and a stability criterion may be derived from the one-dimensional governing equations of the flow. With this criterion, the Ergun pressure drop relation,<sup>11</sup> which is analogous to Equation 3.10, is used to locate regions of positive pressure drop with increasing mass flow. The assumptions made in such analyses seem extreme, however. Stability is based on the behavior of the pressure through the bed, yet the assumption is initially made that there is no pressure variation between the bed inlet and outlet. No such assumptions are made in the analysis presented herein.

### 3.3 Local Stability Analysis

In the local stability analysis the flow quantities in the governing equations presented in Chapter 2 are replaced by quantities of the form  $(A_0 + A')$  where  $A_0$  represents the zeroth order solutions to the flow variables and  $A'$  represents perturbations about these zeroth order solutions. With these substitutions, the governing equations are linearized to yield the following first order approximations:

$$\text{State} \quad \frac{p'}{p_0} = \frac{\rho'}{\rho_0} + \frac{T'}{T_0} \quad (3.24)$$

$$\text{Continuity} \quad \frac{\partial \rho'}{\partial t} + \rho' \frac{\partial u_0}{\partial x} + u_0 \frac{\partial \rho'}{\partial x} + \rho_0 \frac{\partial u'}{\partial x} + u' \frac{\partial \rho_0}{\partial x} + \rho_0 \frac{\partial v'}{\partial y} + \rho_0 \frac{\partial w'}{\partial z} = 0 \quad (3.25)$$

## Momentum

$$\mathbf{x}: \frac{\rho_o}{\varepsilon} \frac{\partial \mathbf{u}'}{\partial t} + \frac{\partial \mathbf{p}'}{\partial \mathbf{x}} + \frac{\mathbf{b}}{\mathbf{K}} \mathbf{u}_o [\rho_o \mathbf{u}' + \rho' \mathbf{u}_o] + \frac{\mu_i}{\mathbf{T}_i^n \mathbf{K}} [\mathbf{n} \mathbf{u}_o \mathbf{T}_o^{(n-1)} \mathbf{T}' + \mathbf{T}_o^n \mathbf{u}'] = 0 \quad (3.26a)$$

$$\mathbf{y}: \frac{\rho_o}{\varepsilon} \frac{\partial \mathbf{v}'}{\partial t} + \frac{\partial \mathbf{p}'}{\partial \mathbf{y}} + \frac{\mathbf{b}}{\mathbf{K}} \rho_o \mathbf{u}_o \mathbf{v}' + \frac{\mu_i}{\mathbf{K}} \left( \frac{\mathbf{T}_o}{\mathbf{T}_i} \right)^n \mathbf{v}' = 0 \quad (3.26b)$$

$$\mathbf{z}: \frac{\rho_o}{\varepsilon} \frac{\partial \mathbf{w}'}{\partial t} + \frac{\partial \mathbf{p}'}{\partial \mathbf{z}} + \frac{\mathbf{b}}{\mathbf{K}} \rho_o \mathbf{u}_o \mathbf{w}' + \frac{\mu_i}{\mathbf{K}} \left( \frac{\mathbf{T}_o}{\mathbf{T}_i} \right)^n \mathbf{w}' = 0 \quad (3.26c)$$

## Energy

$$(\rho c)_m \frac{\partial \mathbf{T}'}{\partial t} + c \left[ \rho' \mathbf{u}_o \frac{\partial \mathbf{T}_o}{\partial \mathbf{x}} + \rho_o \mathbf{u}_o \frac{\partial \mathbf{T}'}{\partial \mathbf{x}} + \rho_o \mathbf{u}' \frac{\partial \mathbf{T}_o}{\partial \mathbf{x}} \right] - k_m \left[ \frac{\partial^2 \mathbf{T}'}{\partial \mathbf{x}^2} + \frac{\partial^2 \mathbf{T}'}{\partial \mathbf{y}^2} + \frac{\partial^2 \mathbf{T}'}{\partial \mathbf{z}^2} \right] = 0. \quad (3.27)$$

In the above equations, the perturbation quantities are replaced by normal mode perturbations with constant amplitude of the form

$$\mathbf{A}'(\mathbf{x}, \mathbf{y}, \mathbf{z}, t) = \mathbf{A} e^{(i\bar{\mathbf{k}} + \omega t)} \quad (3.28)$$

where  $\bar{\mathbf{k}}$  is the wavevector whose components ( $k_x, k_y, k_z$ ) give the wavenumber of the perturbation along the x, y, and z axes and  $\omega = \omega_{Re} + i \omega_{Im}$  where  $\omega_{Re}$  and  $\omega_{Im}$  represent the real and imaginary parts, respectively, of the growth rate of the disturbance. Making this substitution and nondimensionalizing gives the following first order solution:

$$\text{State} \quad \frac{\mathbf{p}}{\mathbf{p}_o} = \frac{\rho}{\rho_o} + \frac{\mathbf{T}}{\mathbf{T}_o} \quad (3.29)$$

## Continuity

$$\left( i \mathbf{k}_x \rho_o + \frac{d\rho_o}{d\mathbf{x}} \right) \mathbf{u} + (i \mathbf{k}_y \rho_o) \mathbf{v} + (i \mathbf{k}_z \rho_o) \mathbf{w} + \left( \omega + \frac{d\mathbf{u}_o}{d\mathbf{x}} + i \mathbf{k}_x \mathbf{u}_o \right) \rho = 0 \quad (3.30)$$

### Momentum

$$\mathbf{x}: \left( \frac{\omega \rho_o}{\varepsilon} \mathbf{Re} + \frac{\mathbf{ReFs}}{\mathbf{Da}} \rho_o \mathbf{u}_o + \frac{\mathbf{T}_o^n}{\mathbf{Da}} \right) \mathbf{u} + \left( \frac{i \mathbf{k}_x \mathbf{Re}}{\gamma \mathbf{M}_i^2} \right) \mathbf{p} + \left( \frac{\mathbf{ReFs}}{\mathbf{Da}} \mathbf{u}_o^2 \right) \rho + \left( \frac{n \mathbf{u}_o \mathbf{T}_o^{(n-1)}}{\mathbf{Da}} \right) \mathbf{T} = 0 \quad (3.30a)$$

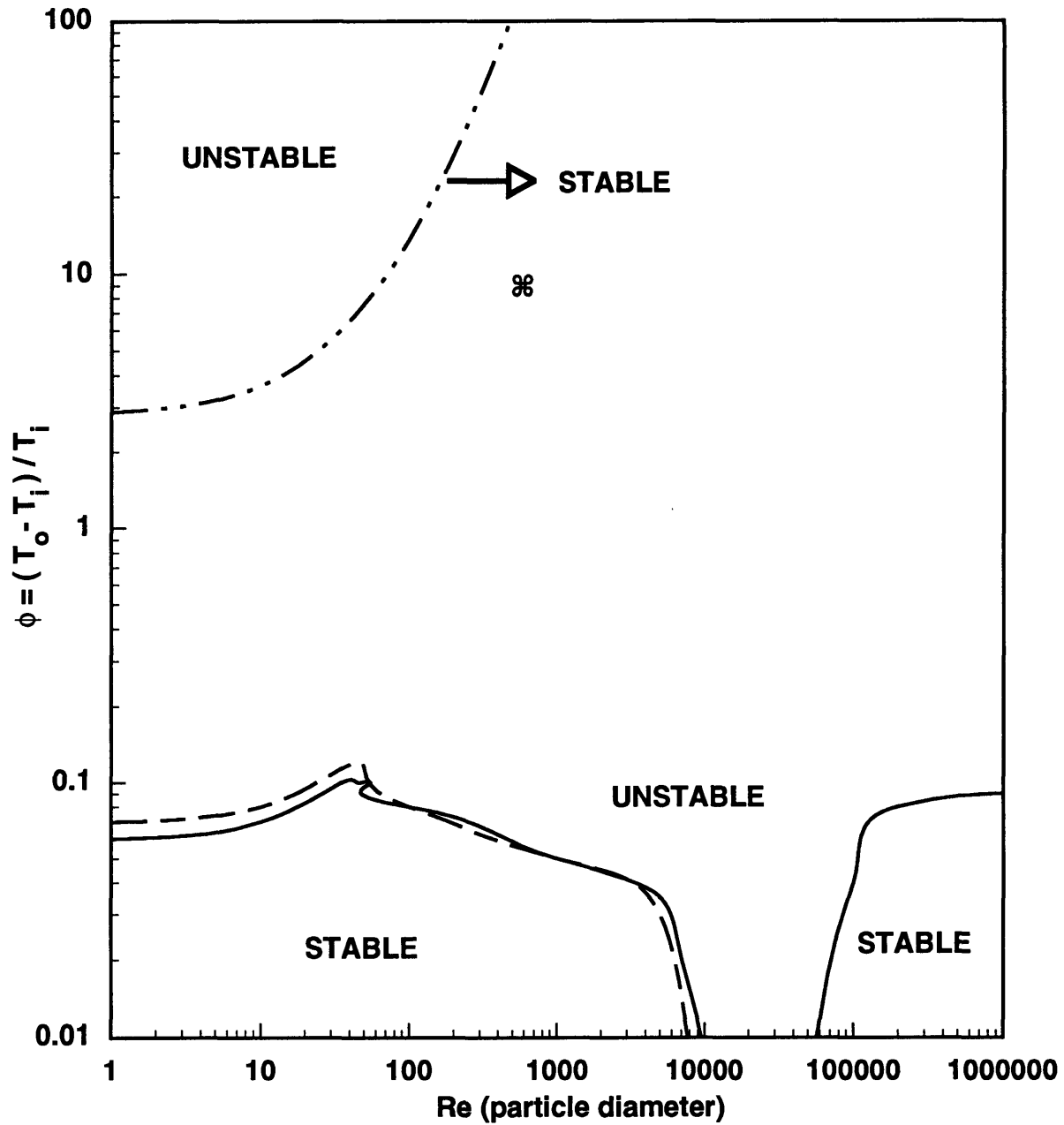
$$\mathbf{y}: \left( \frac{\omega \rho_o}{\varepsilon} \mathbf{Re} + \frac{\mathbf{ReFs}}{\mathbf{Da}} \rho_o \mathbf{u}_o + \frac{\mathbf{T}_o^n}{\mathbf{Da}} \right) \mathbf{v} + \left( \frac{i \mathbf{k}_y \mathbf{Re}}{\gamma \mathbf{M}_i^2} \right) \mathbf{p} = 0 \quad (3.30b)$$

$$\mathbf{z}: \left( \frac{\omega \rho_o}{\varepsilon} \mathbf{Re} + \frac{\mathbf{ReFs}}{\mathbf{Da}} \rho_o \mathbf{u}_o + \frac{\mathbf{T}_o^n}{\mathbf{Da}} \right) \mathbf{w} + \left( \frac{i \mathbf{k}_z \mathbf{Re}}{\gamma \mathbf{M}_i^2} \right) \mathbf{p} = 0 \quad (3.30c)$$

### Energy

$$\left( \rho_o \frac{\partial \mathbf{T}_o}{\partial \mathbf{x}} \right) \mathbf{u} + \left( \mathbf{u}_o \frac{\partial \mathbf{T}_o}{\partial \mathbf{x}} \right) \rho + \left[ \omega \mathbf{S} + i \mathbf{k}_x \rho_o \mathbf{u}_o + \frac{\lambda}{\mathbf{RePr}} (\mathbf{k}_x^2 + \mathbf{k}_y^2 + \mathbf{k}_z^2) \right] \mathbf{T} = 0 \quad (3.31)$$

where  $\mathbf{u}$ ,  $\mathbf{v}$ ,  $\mathbf{w}$ ,  $\mathbf{p}$ ,  $\rho$ , and  $\mathbf{T}$  represent the amplitudes of the flow perturbations. The coefficients of these amplitudes are all determined either as input parameters or solutions to the nondimensionalized zeroth order equations given in Section 3.2. With the above set of equations, the issue of stability may be examined at any point within the bed. To accomplish this, the determinant of the matrix of coefficients of the perturbation amplitudes is equated to zero. For a solution to exist for the above system of equations, this determinant must yield an indicial equation which is not identically equal to zero. This is in fact the case for the above equations. The indicial equation yielded is fifth-order in  $\omega$  and a function of  $\mathbf{k}_x$ ,  $\mathbf{k}_y$ , and  $\mathbf{k}_z$ . To determine stability,  $\mathbf{k}_x$ ,  $\mathbf{k}_y$ , and  $\mathbf{k}_z$  are specified and the roots of the resulting fifth-order polynomial in  $\omega$  are calculated. From the form of the disturbance specified in Equation 3.28, stability is indicated if the real part of  $\omega$  is negative while instability occurs when the real part of  $\omega$  is positive. The results of this analysis for a range of  $\phi$  and  $\mathbf{Re}$  are given in Figure 3.3. The cases presented in



- Parallel Stream
- Bed Inlet  $k_x = k_y = k_z = 1 / \text{cm}$
- - - Bed Exit  $k_x = k_y = k_z = 1 / \text{cm}$
- $\otimes$  Nominal Operating Point at  
40 GW / m<sup>3</sup> with  $T_o = 3000 \text{ K}$

Figure 3.3 Local stability analysis for PBR at the bed inlet and exit.

Figure 3.3 all used as inputs wavenumbers equal to a bed thickness for the x, y, and z directions. This choice was determined to yield the most unstable results for the combinations of wavenumbers examined. The stability boundaries of Figure 3.3 are markedly different from those of the parallel stream analysis. According to the local stability analysis, most of the  $\phi$ - $Re$  space examined is unstable as is the nominal operating point of the bed.

### 3.4 Complete Stability Analysis

Due to the difference between the parallel stream and local stability models, as well as for completeness, a complete stability analysis is needed where boundary conditions as well as the effects of the cold and hot frits are included. The results of the local stability analysis, as mentioned in Section 3.3, are very different from those of the parallel stream model where only the x-dependence of the flow was examined. In the local analysis, all perturbation quantities were assumed harmonic along the x, y, and z axes. This assumption may be the cause of the discrepancies noted above in that the flow perturbations along the x axis may not be harmonic. To examine this possibility, in the complete stability analysis which follows, the perturbations are assigned the new form

$$A'(x, y, z, t) = A(x)e^{i(k_y y + k_z z) + \alpha t} \quad (3.32)$$

to include this x-dependence explicitly in the perturbation amplitude while maintaining the harmonic nature along the y and z axes. Using the above form for the perturbed quantities, the complete analysis is outlined first for the bed alone, then for the cold frit plus the bed, and finally for the entire fuel element including both frits. The details of these analyses follow.

### 3.4.1 Complete Stability Analysis for the Particle Bed Without Frits

As mentioned earlier, to account for the  $x$ -dependence of the perturbation quantities, disturbances of the form in Equation 3.32 are substituted into the first order approximation to the governing flow equations (Equations 3.24-3.27) and after nondimensionalization yield the following set of equations:

$$\text{State} \quad \frac{\mathbf{p}_x}{\mathbf{p}_o} = \frac{\rho_x}{\rho_o} + \frac{\mathbf{T}_x}{\mathbf{T}_o} \quad (3.33)$$

**Continuity**

$$\frac{d\mathbf{u}_x}{dx} = -\frac{1}{\rho_o} \left\{ \left( \frac{d\rho_o}{dx} \right) \mathbf{u}_x + \left( \omega + \frac{d\mathbf{u}_o}{dx} \right) \rho_x + \mathbf{u}_o \frac{d\rho_x}{dx} + \frac{\rho_o [k_y^2 + k_z^2]}{\left[ \frac{\rho_o \omega}{\varepsilon} + \rho_o \mathbf{u}_o \frac{\mathbf{F}s}{\mathbf{D}a} + \frac{\mathbf{T}_o^n}{\mathbf{Re} \mathbf{D}a} \right] \gamma \mathbf{M}_i^2} \mathbf{p}_x \right\} \quad (3.34)$$

**Momentum**

$$\frac{d\mathbf{p}_x}{dx} = -\frac{\gamma \mathbf{M}_i^2}{\mathbf{Re}} \left\{ \left[ \frac{\rho_o \omega}{\varepsilon} \mathbf{Re} + \rho_o \mathbf{u}_o \frac{\mathbf{Re} \mathbf{F}s}{\mathbf{D}a} + \frac{\mathbf{T}_o^n}{\mathbf{D}a} \right] \mathbf{u}_x + \left( \frac{\mathbf{Re} \mathbf{F}s}{\mathbf{D}a} \mathbf{u}_o^2 \right) \rho_x + \left( \frac{n \mathbf{u}_o \mathbf{T}_o^{(n-1)}}{\mathbf{D}a} \right) \mathbf{T}_x \right\} \quad (3.35)$$

**Energy**

$$\frac{\lambda}{\mathbf{Re} \mathbf{Pr}} \frac{d^2 \mathbf{T}}{dx^2} = \left[ \omega \mathbf{S} + \frac{\lambda}{\mathbf{Re} \mathbf{Pr}} (k_y^2 + k_z^2) \right] \mathbf{T}_x + \left( \mathbf{u}_o \frac{d\mathbf{T}_o}{dx} \right) \rho_x + \rho_o \mathbf{u}_o \frac{d\mathbf{T}_x}{dx} + \left( \rho_o \frac{d\mathbf{T}_o}{dx} \right) \mathbf{u}_x \quad (3.36)$$

where  $\mathbf{u}_x$ ,  $\mathbf{p}_x$ , etc. are the amplitudes of the perturbations as a function of  $x$ . The above represent a complex system of equations which is time consuming to solve due to the second order differential in the energy equation. This second order term is thus neglected in the complete analysis as it was in the parallel stream model. Making this approximation, Equation 3.36 becomes

$$\frac{dT_x}{dx} = -\frac{1}{\rho_o u_o} \left[ \omega S + \frac{\lambda}{Re Pr} (k_y^2 + k_z^2) \right] T_x - \left( \frac{1}{u_o} \frac{dT_o}{dx} \right) u_x - \left( \frac{1}{\rho_o} \frac{d\rho_o}{dx} \right) \rho_x. \quad (3.37)$$

Differentiating and manipulating Equation 3.33 using the zeroth order relations from Section 3.2 gives

$$\frac{dp_x}{dx} = \frac{1}{T_o} \frac{dp_x}{dx} - \frac{1}{T_o^2} \frac{dT_o}{dx} \phi p_x - \frac{\rho_o}{T_o} \frac{dT_x}{dx} - \left[ \frac{1}{T_o} \frac{d\rho_o}{dx} - \frac{\rho_o}{T_o^2} \frac{dT_o}{dx} \right] T_x. \quad (3.38)$$

Equations 3.34-35 and 3.37-38 now represent a system of first order linear differential equations in  $x$  for the perturbation amplitudes. To determine the neutral stability boundary, this system of equations is solved using a fourth-order Runge-Kutta technique with inlet boundary conditions  $p_x(0)=0$ ,  $T_x(0)=0$ ,  $\rho_x(0)=0$  and  $u_x(0)=0.01$ . The initial condition for the velocity perturbation is used to scale the solutions. Due to the plenum nature of the PBR design, any pressure perturbations are contained entirely within the bed; consequently, the perturbation in pressure at the outlet, as at the inlet, is given by  $p_x(\text{exit})=0$ . Using these boundary conditions, an iterative procedure is followed whereby  $\phi$  and  $Re$  are varied until the outlet boundary condition on the pressure perturbation is met. Having satisfied the exit condition,  $\omega$  is now varied along with  $\phi$  and  $Re$  until the exit condition is satisfied for  $\omega=0$ , thus giving a point on the neutral stability boundary. The results of this analysis for  $k_m=0$  and 2.5 W/mK are presented in Figure 3.4 along with the earlier results of the parallel stream model for comparison. Figure 3.5 shows characteristic plots of the perturbation quantities as a function of radial position. From Figure 3.4, for  $k_m=0$  the results of the complete analysis are almost identical to those of the parallel stream case. This outcome gives reassurance that the complete model is correct since it uses a very different approach from the parallel stream model yet yields similar results. These results are also verified by a similar analysis by Kerrebrock<sup>12</sup> which was carried out in parallel to this work. The results also indicate that there is a



strong x-dependence to the perturbation quantities which are not harmonic in all cases and may explain the unusual results of the local analysis. It should be noted that the disturbance wavenumbers in the y and z directions were chosen to be 1 per bed thickness(1/cm) in this and subsequent analyses. This choice was found to yield the most unstable behavior by the local analysis. It is possible, however, that certain combinations of wavenumbers not explored in the local model may lead to instances of greater instability. By introducing conductivity the bed is slightly more stable at high **Re**(>20) and significantly more stable at low **Re**. This behavior is very different at low **Re** from that predicted by the parallel stream analysis.

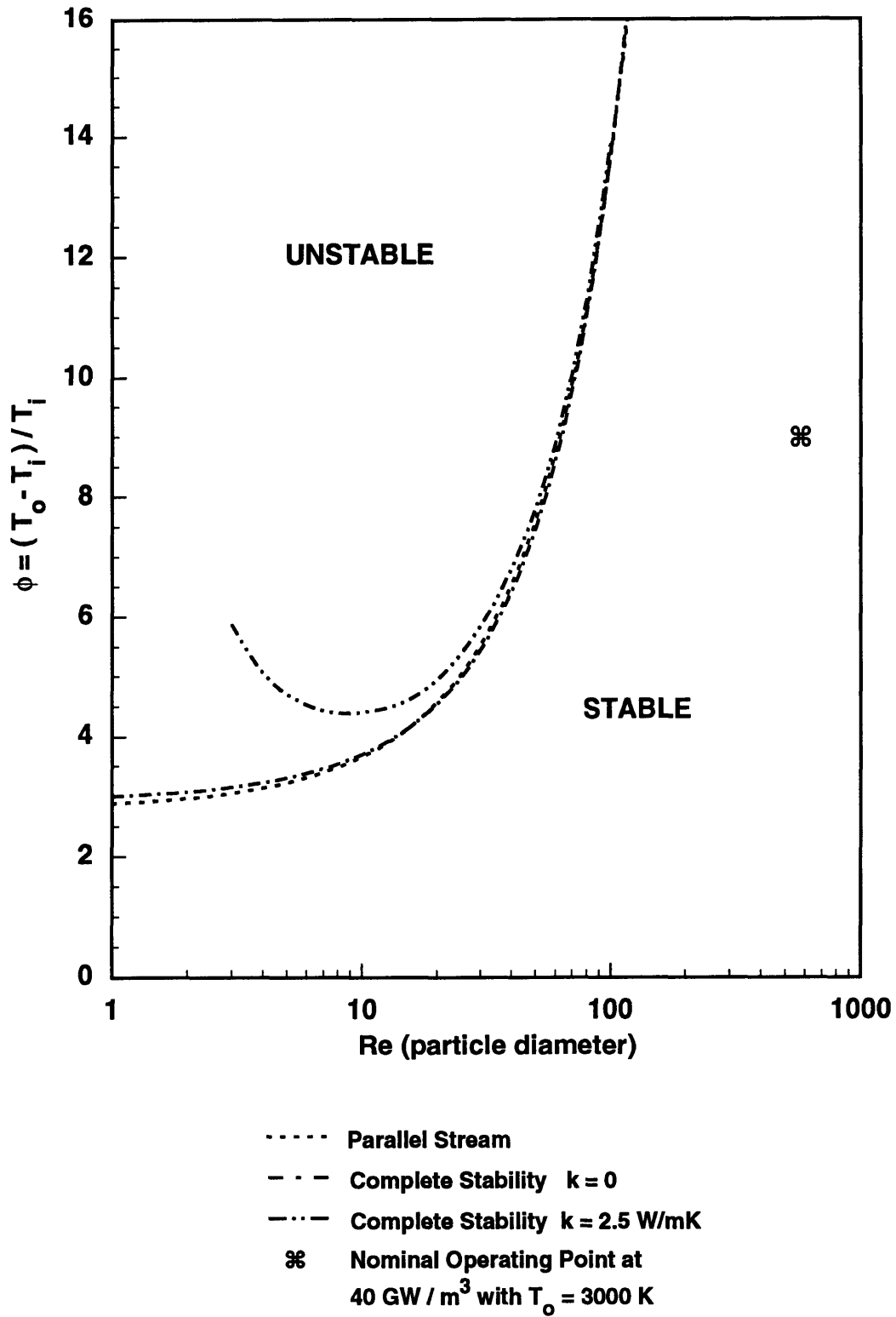
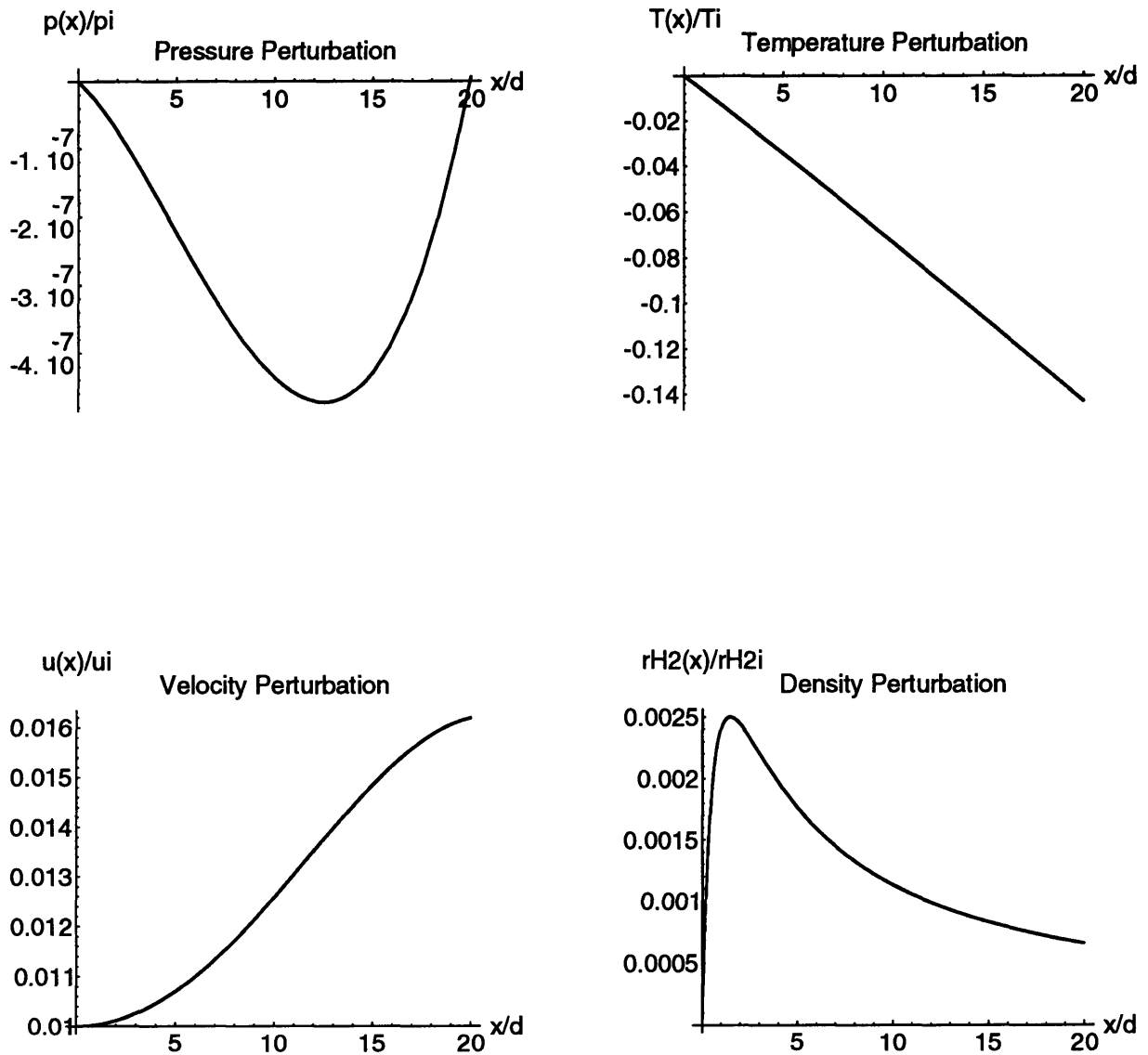


Figure 3.4 Complete stability analysis of particle bed for  $k_m=0$  and 2.5 W/mK.



**Figure 3.5** Radial dependence of perturbation quantities calculated by complete analysis for the case  $k_m=0$ ,  $\omega=0$ ,  $\phi=13.7$ ,  $Re=100$ . Note the quantities  $p(x)$ ,  $T(x)$ ,  $u(x)$ , and  $rH_2(x)$  coincide with the perturbation amplitudes  $p_x$ ,  $T_x$ ,  $u_x$ , and  $\rho_x$  respectively of Equations 3.33-3.36. The quantities  $p_i$ ,  $T_i$ ,  $u_i$ , and  $rH_{2i}$  coincide with the bed inlet flow quantities  $p_i$ ,  $T_i$ ,  $u_i$ , and  $\rho_i$  respectively.

### 3.4.2 Complete Stability Analysis for the Particle Bed Including the Cold Frit

For the purpose of generating a more realistic model, the impact to stability with the introduction of a cold frit on the inlet side of the bed is explored. A similar method to that detailed in §3.4.1 is used to model the flow through the cold frit. The frit is assumed to be made of aluminum with  $\varepsilon=0.4$ ,  $\ell=0.0015$  m,  $c_{Al}=800$  J/kg K,  $k_{Al}=237$  W/mK, and  $k_m=237(1-\varepsilon)$  W/mK. The assumption is also made that  $q=0$  within the frit.

With the assumption of no volumetric heat addition within the cold frit, the zeroth order energy equation (Equation 3.16) yields the following:

$$\frac{dT_o}{dx} = 0 \quad (3.39)$$

$$T_o = 1. \quad (3.40)$$

The inlet Mach number is also modified by the above assumption and is given below:

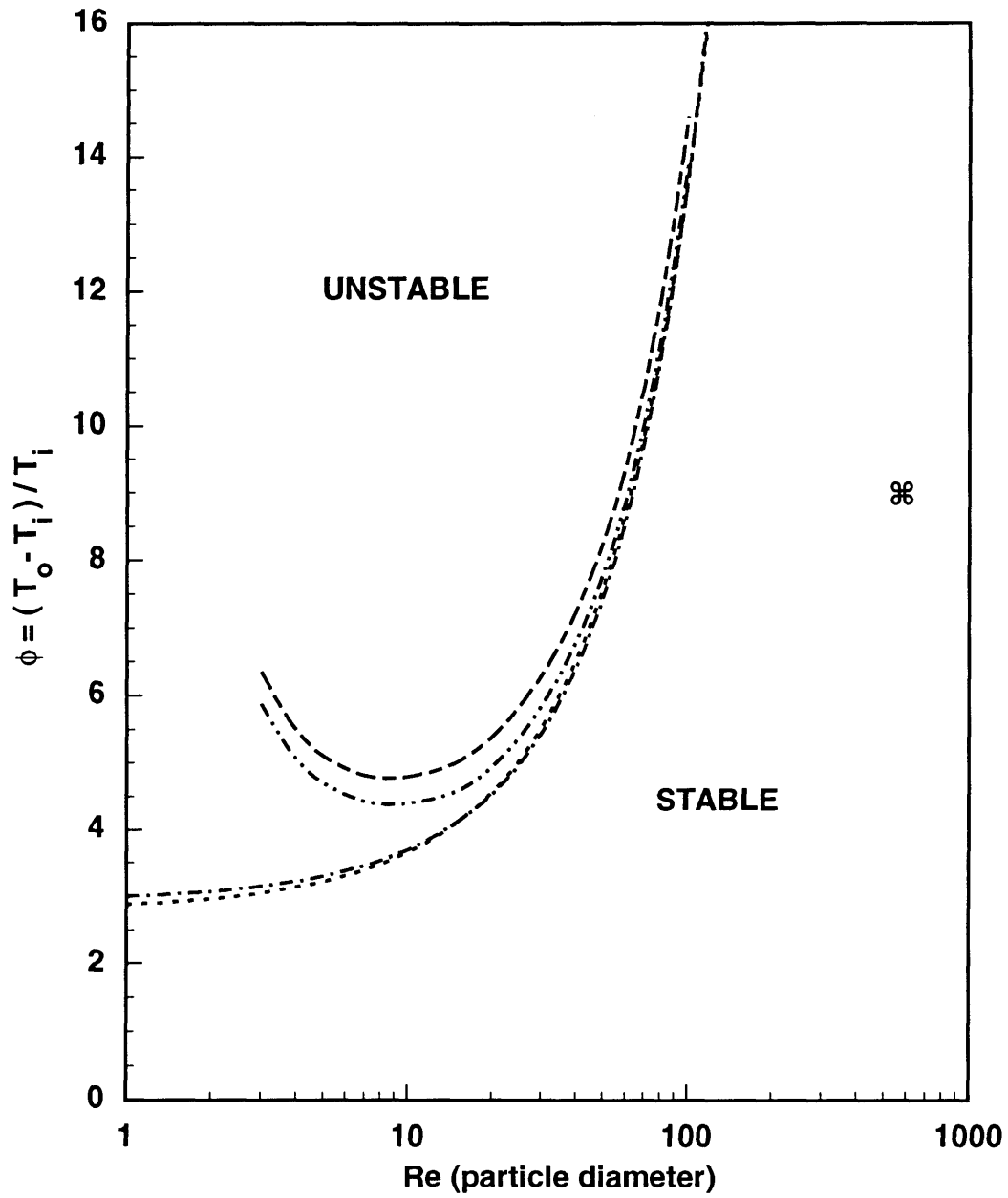
$$M_i = \frac{\sqrt{\gamma R T_i} \text{Re} \mu_i}{\gamma p_i d}. \quad (3.41)$$

Using Equations 3.39-3.41, the zeroth order and first order equations used for the particle bed in §3.4.1 are modified for the cold frit. The majority of these changes are straightforward and are not detailed here. However, with no x-dependence on the temperature through the cold frit, the zeroth order pressure equation and first order perturbed momentum equation are significantly modified and thus given by Equations 3.42 and 3.43 respectively:

$$p_o^2 = 1 - 2\gamma M_i^2 \left( \frac{1}{\text{Re Da}} + \frac{Fs}{\text{Da}} \right) x \quad (3.42)$$

$$\frac{dp_x}{dx} = -\frac{\gamma M_i^2}{\text{Re}} \left\{ \left[ \frac{\rho_o \omega}{\varepsilon} \text{Re} + \frac{\text{Re} Fs}{\text{Da}} + \frac{1}{\text{Da}} \right] u_x + \left( \frac{\text{Re} Fs}{\text{Da}} u_o^2 \right) \rho_x \right\}. \quad (3.43)$$

With the above changes, the governing equations for the cold frit are solved in a similar manner to those for the particle bed. The initial conditions used are the same as those for the bed, but in this case were applied at the inlet to the cold frit. Using these initial conditions, the radial dependence of the perturbation quantities through the cold frit is calculated for  $\omega=0$  and a range of  $Re$ . The calculated values for these perturbations at the outlet to the frit for a given  $Re$  are then used as initial conditions at the bed inlet. With these initial conditions now specified for a given  $Re$  and  $\omega=0$ , the governing equations for the particle bed are solved for an initial value of  $\phi$ . As before, the constraint at the outlet of the bed is  $p_x(\text{exit})=0$ ; consequently,  $\phi$  is varied until this outlet condition is satisfied thus giving a point on the neutral stability boundary. Typical results for the radial dependence of the perturbation quantities through the cold frit and particle bed are similar to those of Figure 3.5. Figure 3.6 presents the neutral stability boundary derived in this case along with those derived earlier for comparison. From Figure 3.6, the addition of the cold frit tends to stabilize over the range of  $Re$  examined with more stabilization occurring at  $Re < 30$ .



- ..... Parallel Stream
- - - Complete Stability  $k = 0$
- · - Complete Stability  $k = 2.5 \text{ W/mK}$
- - - Complete Stability  $k = 2.5 \text{ W/mK}$   
with Al cold frit
- ⊗ Nominal Operating Point at  
 $40 \text{ GW} / \text{m}^3$  with  $T_o = 3000 \text{ K}$

Figure 3.6 Complete stability analysis of particle bed and cold frit for  $k_m = 2.5 \text{ W/mK}$ .

### 3.4.3 Complete Stability Analysis for the Particle Bed Including Both Frits

To finalize the flow stability model for the PBR, both the cold and hot frit are added to the bed. In the case of the hot frit, as with the cold frit, the assumption is made that  $q=0$ . This assumption leads to the following results from the zeroth order energy equation:

$$\frac{dT_o}{dx} = 0 \quad (3.44)$$

$$T_o = \phi + 1 \quad (3.45)$$

where the zeroth order temperature through the hot frit is the exit temperature of the particle bed. As with the cold frit, these results are used to modify the governing equations for the bed to determine the flow equations for the hot frit. The hot frit is assumed to be made of graphite with  $\varepsilon=0$ ,  $\ell=0.003$  m,  $c_{Gr}=1884$  J/kgK,  $k_{Gr}=41.87$  W/mK, and  $k_m=41.87(1-\varepsilon)$  W/mK.

The solution procedure of the boundary value problem with the inclusion of the hot frit is similar to that used in §3.4.2. As before, the inlet boundary conditions are taken at the cold frit inlet. For a specified  $Re$  and  $\omega=0$ , the radial dependence of the perturbation quantities in the cold frit is calculated using a standard fourth-order Runge-Kutta technique. The outlet conditions at the cold frit are then used as the inlet conditions to the particle bed. With the inlet conditions specified for the particle bed, the perturbation quantities are calculated through the bed for  $\omega=0$ , the specified  $Re$ , and an initial value for  $\phi$ . The perturbation values calculated at the bed exit are then used as the inlet values for the hot frit governing equations. Once again, for  $\omega=0$  and the specified  $Re$ , the radial dependence of the perturbation quantities is calculated through the hot frit. As in the previous analyses, the boundary condition at the exit of the hot frit is  $p_x(\text{exit})=0$ . If this condition is not satisfied by the calculated pressure perturbation, an

iterative procedure is followed whereby the bed and hot frit equations are solved for various values of  $\phi$  until the exit boundary condition is satisfied, thus yielding a point on the neutral stability boundary. Again the radial dependence of the perturbation quantities is similar to that of Figure 3.5 with the neutral stability boundaries for this and previous cases shown in Figure 3.7.



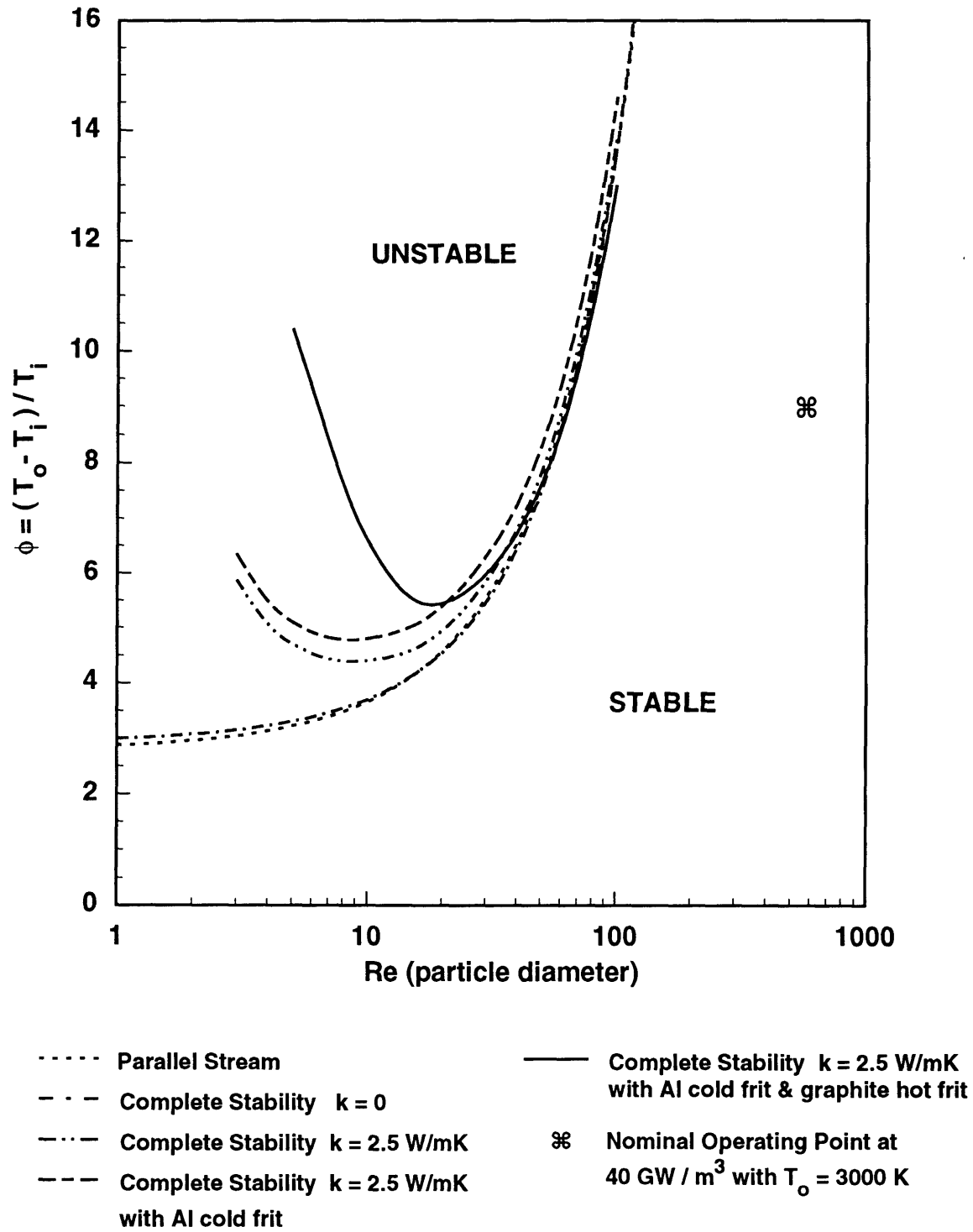


Figure 3.7 Complete stability analysis of particle bed and both frits for  $k_m = 2.5 \text{ W/mK}$ .

## Chapter 4

### Comparison of Stability Model to Experimental Results

To date there has been little experimental research on the flow instability of an actual PBR element. The research which has been conducted has been either inconclusive or only qualitative in nature. Recently, Conley <sup>13</sup> performed a qualitative experiment in which a cylindrical column of SiC beads was heated using microwaves with nitrogen gas flow introduced. The results indicate that local areas of high temperature may develop within a particle bed implying some sort of a flow anomaly. During the summer of 1992, Lawrence performed the most quantitative test to date on a simulated particle bed element at Brookhaven National Laboratory <sup>14</sup>. In this experiment, titled the flow instability test(FIT), the particle bed was constructed from a highly resistive stainless steel mesh which was rolled to form a cylindrical particle bed and was then heated electrically. The bed was instrumented with a series of thermocouples to measure variations in bed temperatures for various flow conditions. With He as the propellant, a series of experiments were conducted in which  $\phi$  and  $Re$  for the bed were varied. Lawrence noted divergences in temperature between thermocouples within the bed for various flow conditions.

Using the material properties for Lawrence's bed along with the properties of He, the parallel stream model of Section 3.2 and complete stability analysis of §3.4.1 were

repeated for the FIT configuration and are given in Figure 4.1 along with a sampling of data from the FIT experiment. The results of the models presented in Figure 4.1 for He are similar to those for hydrogen presented in Chapter 3. With the introduction of bed thermal conductivity, which in the case of the Brookhaven bed was calculated to be 12 W/mK, the complete model predicts stability throughout most of the  $\phi$ -Re space examined. The model does not include frits, which Lawrence's test did include, but from the results of §3.4.2-3.4.3, their inclusion should add to the stability of the bed.

Lawrence's data represent points in  $\phi$ -Re space for diverging temperatures between thermocouples within the bed. These data lie near the parallel stream stability curve, but according to the complete model, should not be in the unstable flow regime. The question then must be asked if in fact these points represent flow instability. Granted, the model used here is a plane-parallel model whereas the experiment used a cylindrical geometry. Also, as mentioned earlier, flow stability is very sensitive to bed thermal conductivity; consequently, a poor estimate of the FIT bed conductivity could significantly change the stability boundaries. However, for the model to agree with the FIT results, the FIT bed thermal conductivity would have to be almost zero, which seems unlikely considering the bed is made of stainless steel wire. The issue of geometry should also be a minor distinction. A more likely explanation of Lawrence's data may lie in the FIT bed itself. The local hot spots may have something to do with the seams which Lawrence mentions are present within the bed. These seams may cause local areas of the bed to be starved for flow, which could explain the thermocouple discrepancies noted in the data. In the final analysis, however, all these issues indicate a need for more experimental research on flow instability in PBRs.

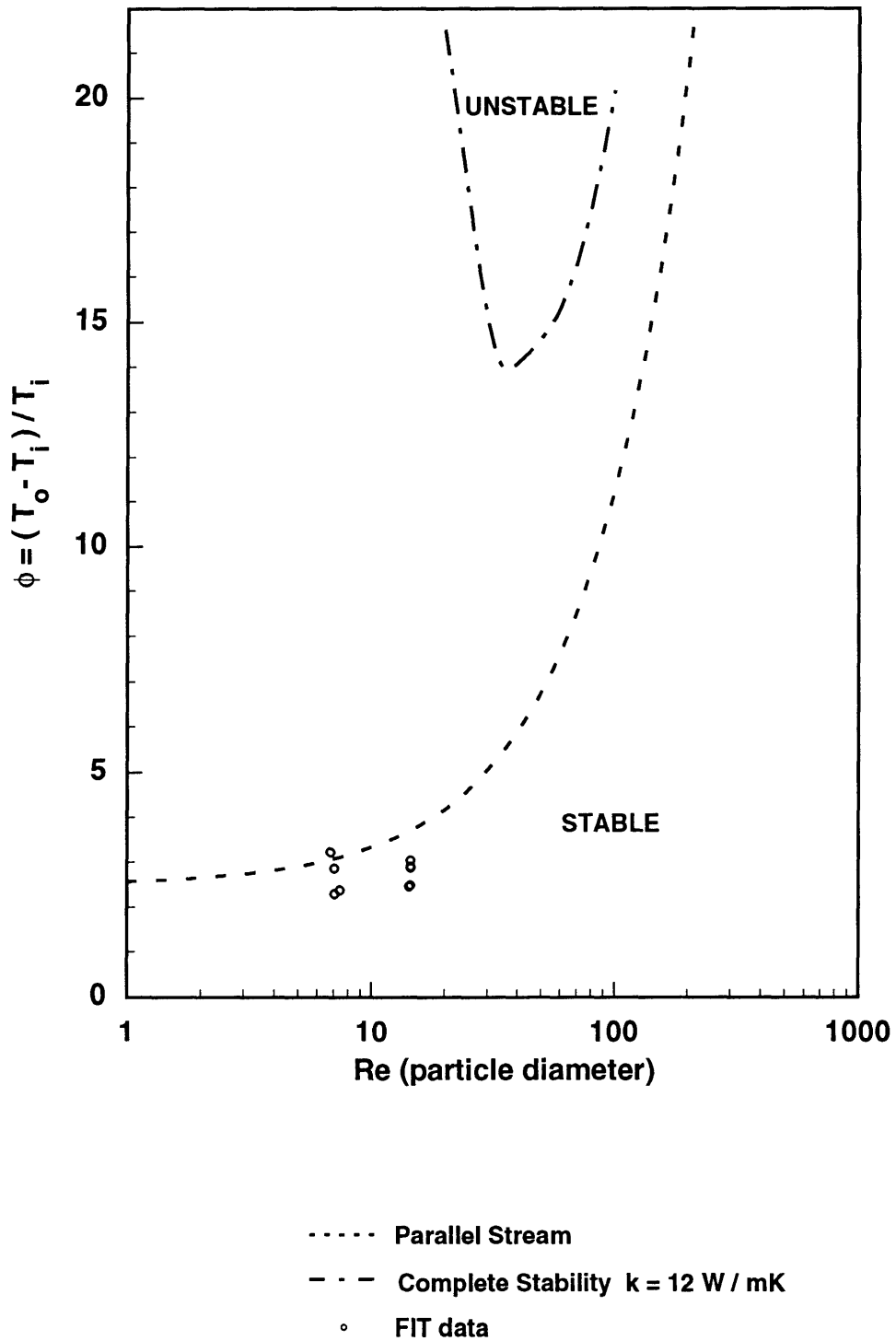


Figure 4.1 Comparison of parallel stream and complete stability models to FIT data.

## Chapter 5

### Conclusions and Recommendations for Future Work

The results of this work indicate that the PBR is subject to flow instability at low  $Re$  and high  $\phi$ , but is stable at the nominal operating point of  $40 \text{ GW/m}^3$ . The region of instability is found to agree qualitatively with results obtained by other researchers for the case where the effective thermal conductivity of the particle bed is assumed negligible. However, the complete stability model presented here predicts significant stabilization of the bed (especially at  $Re < 30$ ) with increased bed conductivity. This result is not surprising considering increased thermal conductivity aids in distributing heat throughout the bed and thus alleviates local hot spots; yet until now, this additional stabilization at low  $Re$  had not been considered. Bed stability is also found to increase significantly at low  $Re$  with the inclusion of frits. The complete analysis indicates that the inclusion of a cold frit tends to stabilize somewhat at low  $Re$ , due to the pressure drop introduced by the frit. With the inclusion of the hot frit as well, the analysis indicates a significant stabilizing effect at low  $Re$ . This stabilization is probably due to the added heat distribution provided by the hot frit by way of its higher thermal conductivity and the assumption of no volumetric heat addition. These results indicate that the use of frits should allow stable operation of the bed over the entire sequence of startup to full power operation. Nevertheless, it is important to recognize that regions of instability can exist, and as such, should be avoided during all phases of PBR operation.

As mentioned earlier, the models presented here are for a plane-parallel approximation of a fuel element. In practice, PBR fuel elements are cylindrical in nature, and in some cases, have variable-area channels. Consequently, to better model the fuel element, the governing equations used in the analyses should be rewritten in cylindrical coordinates and the analyses repeated. Several other assumptions are made in the models; most notably, the volumetric heat addition in the bed is assumed constant and the effective conductivity of the bed is estimated from the conductivity of the fuel particles. In actuality, with the large temperature variations through the fuel element, the fission cross-section of the uranium in the  $UC_2$  particles may vary significantly, thus affecting the volumetric heat addition through the element. Also, due to the point contacts between the particles, an effective conductivity for the particle bed must be measured or calculated because as was shown in this work, the conductivity is a major factor in determining stability. Finally, transient flow models for the particle bed may also be investigated to describe fuel element behavior at start-up and shut-down. Even with these modifications and new approaches, truly characteristic results for particle bed flow stability will only be achieved when a specific design exists for which a model may be tailored. To verify the accuracy of such a model, experimental data for this specific element must then be provided.

## **Appendix A**

### **Mathematica Code**

The solutions to the governing flow equations for the various models presented herein were obtained using the Mathematica® version 2.1.0.2 software package for the Macintosh computer. A representative code for the complete stability analysis is provided in this appendix.

**PARTICLE BED REACTOR**  
**Complete Stability Analysis 7 JULY 1993**  
**Disturbance of the form  $A' = A(x) \exp\{i(k_y + k_z) + \omega t\}$**

$\phi=13.69$   $Re=100$  scaling  $u[0] = .01$

$k_m = 0$

**Kalamas**

■ **Input Parameters**

```
f=13.69;  
Rd=100;  
e=0.4;  
km=0;  
kg=.182;  
rm=5662;  
cm=1300;  
cp=14305;  
Ti=300;  
mi=9*10^-6;  
d=.0005;  
g=1.409;  
pi=6080000;  
K=3*10^-10;  
b=10^-5;  
R=4157;  
n=.667;  
lb=.01;  
x=.
```

```
q= f Rd cp Ti mi/(d lb)
```

■ **Dimensionless Parameters**

```
M=((g-1)/g) q .01/(f pi (g R Ti)^.5);  
Fs=b/d;  
Da=K/d^2;  
l=km/kg;  
Pr=mi cp/kg;  
S=rm cm R Ti/(pi cp);
```



■ **Nondimensionalized Zeroth Order Quantities (  $p_o$ ,  $dp_o/dx$ ,  $T_o$ ,  $dT_o/dx$ ,  $\rho_{H2o}$ ,  $d\rho_{H2o}/dx$ ,  $u_o$ ,  $du_o/dx$ )**

$$p_{o2} = -R / (\pi^2 K) * (.75 ((f \, d \, x / lb + 1)^{(n+2)} - 1) \\ * q \, lb^2 \, mi / (cp \, f^2) \\ + ((f \, d \, x / lb + 1)^2 - 1) \, b \, q^2 \, lb^3 / (cp^2 \, Ti \, f^3)) \\ + 1;$$

$$p_o = p_{o2}^{(0.5)};$$

$$dp_o = -R \, d / (p_o \, \pi^2 \, K) * (((f \, d \, x / lb + 1)^{(n+1)}) \\ * q \, lb \, mi / (cp \, f) \\ + (f \, d \, x / lb + 1) \, b \, q^2 \, lb^2 / (cp^2 \, Ti \, f^2));$$

$$T_o = f \, d \, x / lb + 1;$$

$$dT_o = f \, d / lb;$$

$$r_{H2o} = p_o / T_o;$$

$$dr_{H2o} = (dp_o - d \, f \, r_{H2o} / lb) / T_o;$$

$$u_o = 1 / r_{H2o};$$

$$du_o = - dr_{H2o} / (r_{H2o}^2);$$

■ **Nondimensionalized Perturbation Parameters [ growth rate ( $\omega$ ) and transverse wave numbers ( $k_y$ ,  $k_z$ ) ]**

$$w = 0;$$

$$k_y = .05;$$

$$k_z = .05;$$

### ■ Nondimensionalized Perturbed Governing Equations to First Order

```
A=NDSolve[{u'[x] == -((w + duo) rH2[x] + uo rH2'[x]
+ drH2o u[x]
+ rH2o (ky^2 + kz^2) p[x]/((Fs/Da
+ ((f d x/lb+1)^n)/
(Rd Da)) g M^2))/rH2o,
```

```
rH2'[x] == p'[x]/To - d f p[x]/(lb To^2)
- rH2o T'[x]/To - (drH2o/To
- rH2o d f/(lb To^2)) T[x],
```

```
p'[x] == - g M^2/Rd ((Rd Fs/Da
+ ((f d x/lb+1)^n)/Da) u[x]
+ Rd Fs uo^2 rH2[x]/Da
+ n uo ((f d x/lb+1)^(n-1))/
Da T[x]),
```

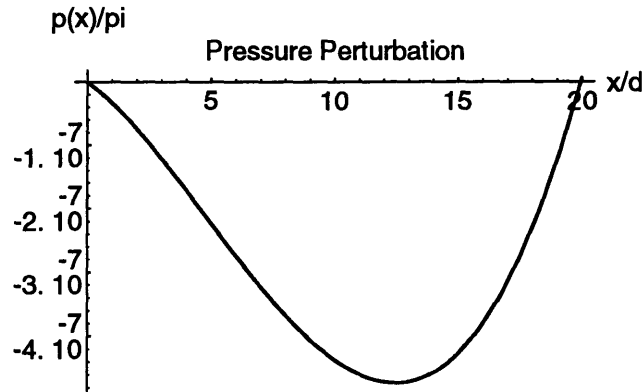
```
T'[x] == -(S w T[x]
+ uo f d rH2[x]/lb
+ rH2o f d u[x]/lb),
```

```
p[0]==0, T[0]==0, rH2[0]==0, u[0]==.01},
{p, T, rH2, u}, {x, 0, 20}]
```

```
{{p -> InterpolatingFunction[{0., 20.}, <>],
T -> InterpolatingFunction[{0., 20.}, <>],
rH2 -> InterpolatingFunction[{0., 20.}, <>],
u -> InterpolatingFunction[{0., 20.}, <>]}}
```

### ■ Perturbation Quantities as a function of x/d

```
Xp=Plot[Evaluate[ p[x]/.A], {x, 0, 20},
AxesOrigin->{0,0},
AxesLabel->{"x/d", "p(x)/pi"},
DefaultFont->{"Helvetica",10},
PlotLabel->"Pressure Perturbation"]
```

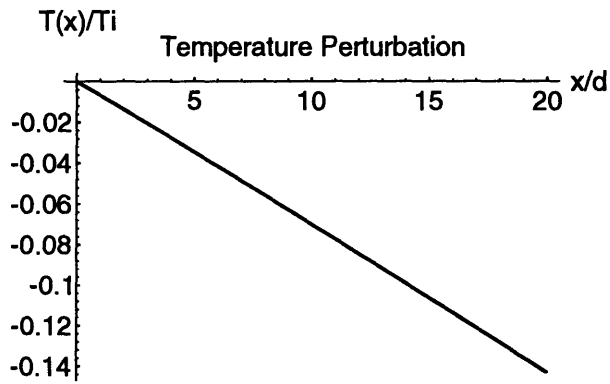


-Graphics-

```

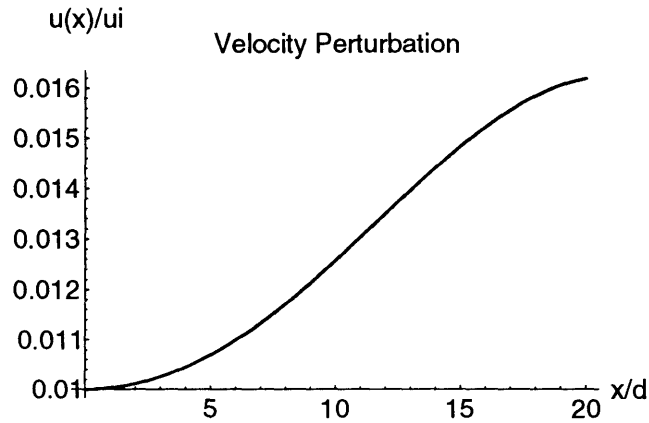
XT=Plot[Evaluate[ T[x]/.A], {x, 0, 20},
  AxesOrigin->{0,0},
  AxesLabel->{"x/d", "T(x)/Ti"},
  DefaultFont->{"Helvetica",10},
  PlotLabel->"Temperature Perturbation"]

```



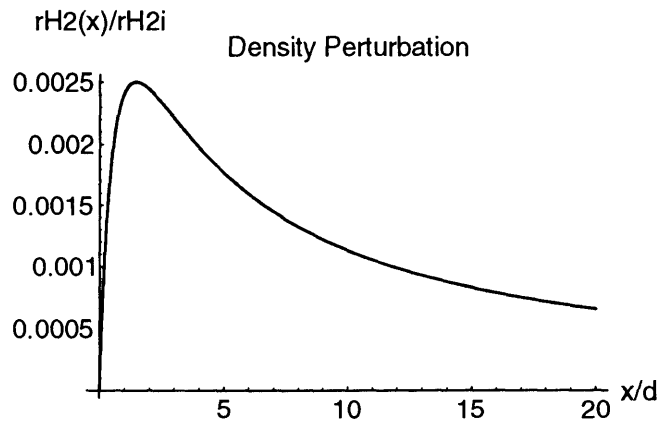
-Graphics-

```
Xu=Plot[Evaluate[ u[x]/.A], {x, 0, 20},
  AxesOrigin->{0,0.01},
  AxesLabel->{"x/d", "u(x)/ui"},
  DefaultFont->{"Helvetica",10},
  PlotLabel->"Velocity Perturbation"]
```



-Graphics-

```
Xd=Plot[Evaluate[ rH2[x]/.A], {x, 0, 20},
  AxesLabel->{"x/d", "rH2(x)/rH2i"},
  DefaultFont->{"Helvetica",10},
  PlotLabel->"Density Perturbation"]
```



-Graphics-

## Bibliography

1. Zubrin, Robert M. "Nuclear Rocket Utilizing Indigenous Martian Fuel(NIMF)." NASA Nuclear Propulsion Workshop/NTP. Cleveland, Ohio: Lewis Research Center: July 10-12, 1990.
2. Lazareth, O. W. , K. J. Araj, F. L. Horn, H. Ludewig, and J. R. Powell. "Analysis of the Start-up and Control of a Particle Bed Reactor." *Space Nuclear Power Systems 1987*. (Malabar, Florida: Orbit Book Company, 1988). pp. 223-227.
3. Ludewig, H. "Particle Bed Reactor Based Nuclear Rocket Concept." NASA Nuclear Propulsion Workshop/NTP. Cleveland, Ohio: Lewis Research Center: July 10-12, 1990.
4. Farbman, G. H. and B. L. Pierce. "The Enabler(Based on Proven NERVA Technology." NASA Nuclear Propulsion Workshop/NTP. Cleveland, Ohio: Lewis Research Center: July 10-12, 1990.
5. Prasad, V. and N. Kladias. "Non-Darcy Natural Convection in Saturated Porous Media." *Proceedings of the NATO Advanced Study Institute on Convective Heat and Mass Transfer in Porous Media*. ed. by S. Kakaç, B. Kilkis, F. A. Kulacki, and F. Arinç. Çesme, Izmir, Turkey. August 6-17, 1990. pp. 173-224.
6. Charmchi, M. , J. W. McKelliget, M.. Rand, and G. Maise. "Thermo-Hydraulic Characteristics of Gas-Cooled Particle Bed Reactors." *Proceedings of the Fourth International Topical Meeting on Nuclear Reactor Thermal-Hydraulics(NURETH-IV)*. Vol. 1. Karlsruhe, FRG. 1989. pp. 139-145.
7. Maise, G. "Flow Stability in the Particle Bed Reactor." Brookhaven National Laboratory, Informal Report BNL/RSD-91-002. January 16, 1991.
8. Prasad, V. "Convective Flow Interaction and Heat Transfer Between Fluid and Porous Layers." *Proceedings of the NATO Advanced Study Institute on*

*Convective Heat and Mass Transfer in Porous Media.* ed. by S. Kakaç, B. Kilkis, F. A. Kulacki, and F. Arinç. Çesme, Izmir, Turkey. August 6-17, 1990. pp. 563-615.

9. Bussard, R. W. and R. D. DeLauer. *Nuclear Rocket Propulsion*(New York: McGraw-Hill, 1958). pp. 129-133.
10. Witter, J. K. , D. D. Lanning, and J. E. Meyer. "Flow Stability Analysis of a Particle Bed Reactor Fuel Element." *Proceedings of the 10th Symposium on Space Nuclear Power and Propulsion. CONF-930103.* M. S. Genk and M. D. Hoover, eds(New York: American Institute of Physics, 1993), p 1541.
11. Ergun, S. "Fluid Flow Through Packed Columns." *Chemical Engineering Progress.* 48-2. 1952. pp. 89-92.
12. Kerrebrock, J. L. and J. Kalamas. "Flow Instability in Particle-Bed Nuclear Reactors." to be presented at AIAA/SAE/ASME/ASEE 29th Joint Propulsion Conference and Exhibit. AIAA 93-1758. Monterey, California. June 28-30, 1993.
13. Conley, B. R. "Experimental Modeling of a Particle Bed Nuclear Rocket." presented at the AIAA Northeast Regional Student Conference. MIT: Cambridge, Massachusetts. April 3, 1993.
14. Lawrence, T. J. "Flow Instability Test for a Particle Bed Nuclear Thermal Rocket Fuel Element." Massachusetts Institute of Technology: Department of Nuclear Engineering Master's Thesis. May, 1993.